Electronic Supplementary Information (ESI)

Super-Hydrophilic Leaflike Sn_4P_3 on the Porous Seamless Graphene–Carbon Nanotube Heterostructure as an Efficient Electrocatalyst for Solar-Driven Overall Water Splitting

Sk Riyajuddin[a], Mansi Pahuja[a], Parrydeep Kaur Sachdeva[a], Kashif Azmi[a], Sushil Kumar[a], Mohd Afshan[a], Firdaus Ali[a], Jenifar Sultana[a], Takahiro Maruyama[b], Chandan Bera[a], and Kaushik Ghosh[a]*

[a] Institute of Nano Science & Technology, Knowledge City, Sector-81, SAS Nagar,140306, Mohali, Punjab, India

[b] Department of Applied Chemistry, Meijo University, 1-501 Shiogamaguchi, Tempaku, Nagoya 468-8502, Japan

***Corresponding Author email: kaushik@inst.ac.in**

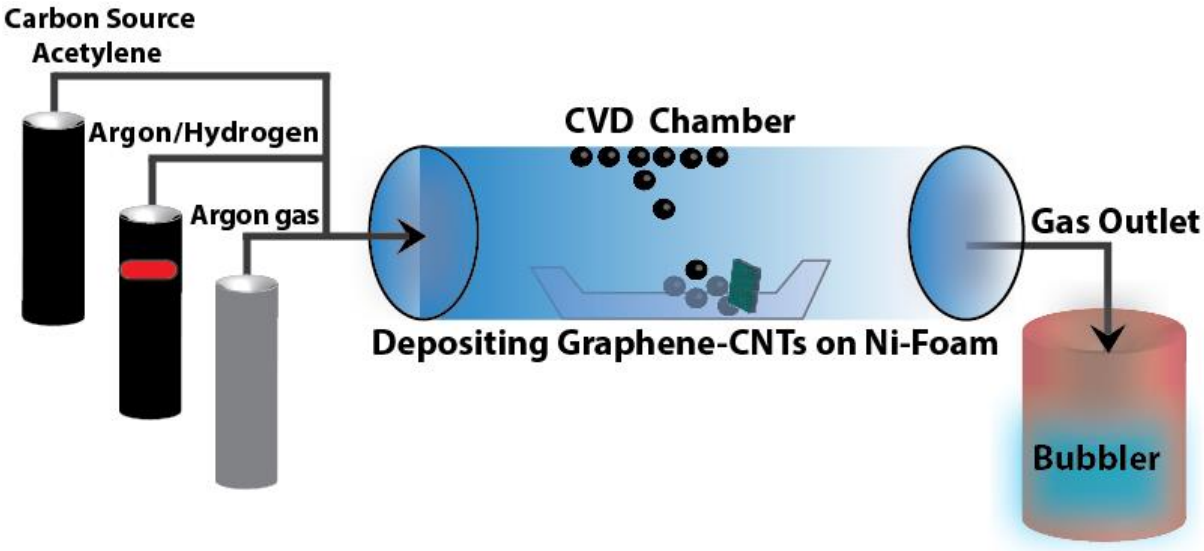

Figure S1. Schematic illustration of the synthesis of Graphene-CNTs on 3D porous Ni-foam by CVD method.

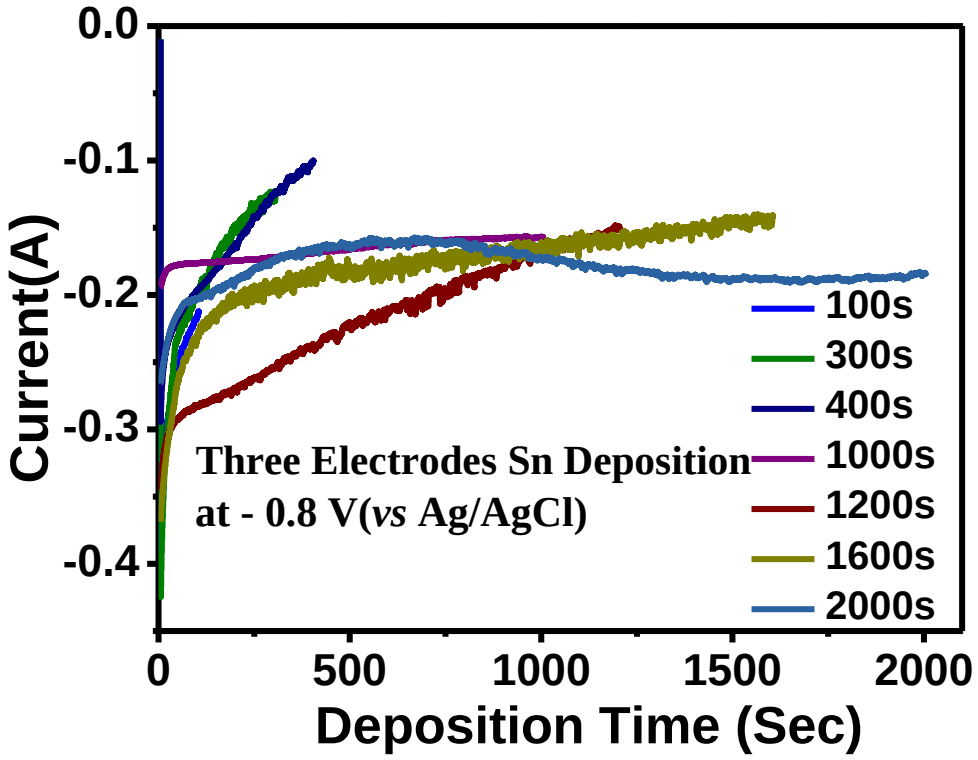

Figure S2. Chronoamperometric deposition of Sn on Ni-Gr-CNTs heterostructure in the three-electrode system at an applied voltage of -0.8 V (*vs* Ag/AgCl) with varying deposition time of 100s to 2000s.

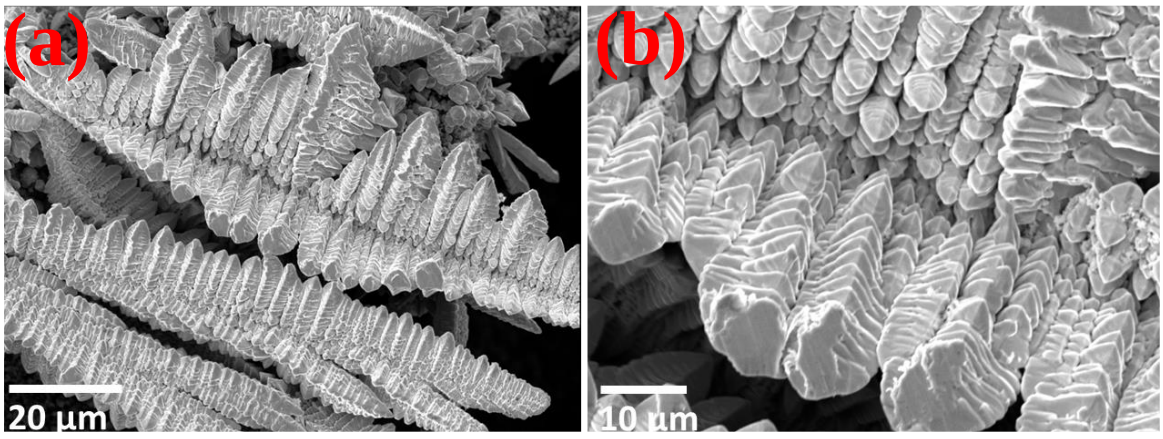

Figure S3. SEM image of Sn_4P_3 on top of Ni-Gr-CNTs matrix where cactus-like structure clearly been observed.

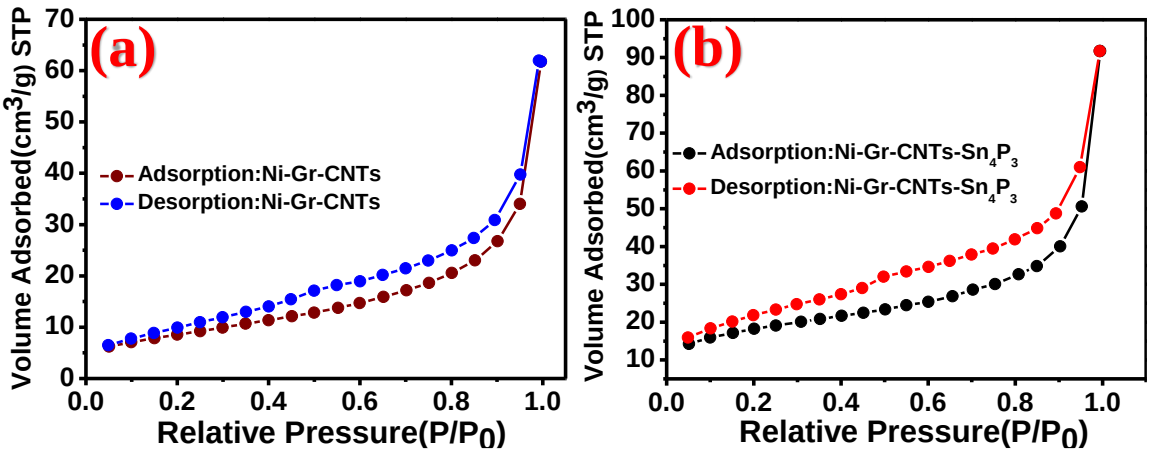

Figure S4. Nitrogen adsorption-desorption isotherm of (a) Ni-Graphene-CNTs and (b) Ni-Graphene-CNTs-Sn_4P_3 sample which indicates significant improvement of the surface area after the decoration of leaf-like Sn_4P_3 on Ni-Gr-CNTs heterostructure.

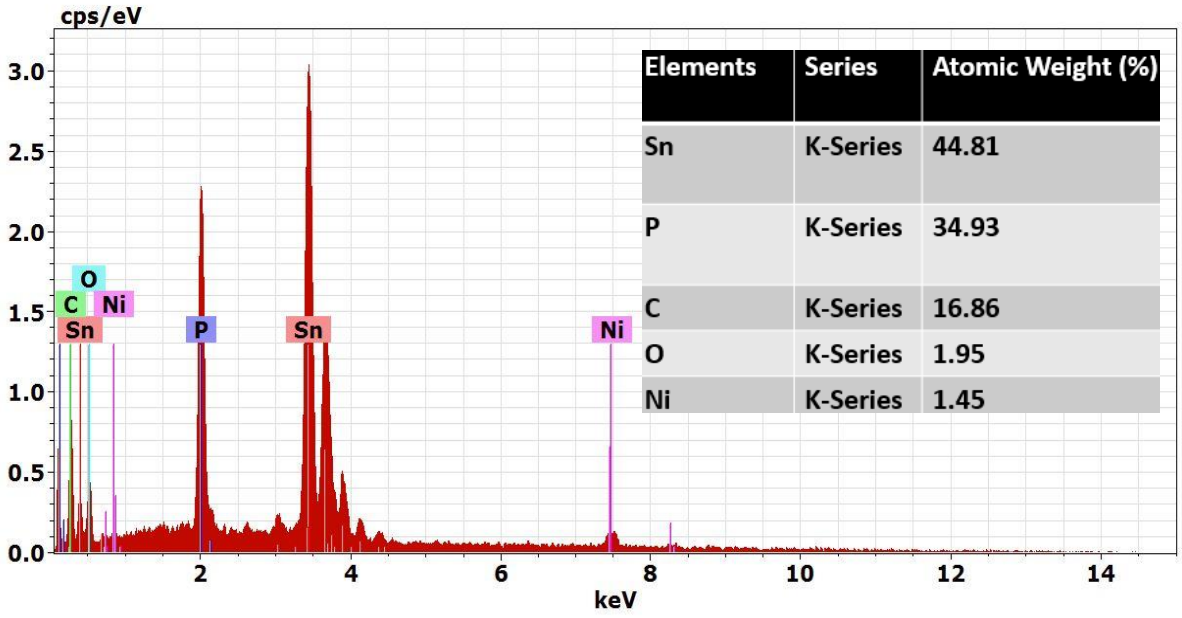

Figure S5. EDX spectrum and elemental percentages (inset) of Ni-Gr-CNTs-Sn_4P_3. The atomic percentage ratio of Sn and P indicates the formation of Sn_4P_3 in the as-grown matrix. A very small percentage of the oxygen may be attributed to the surface oxidation of the as-deposited metal phosphides.

XPS Analysis:

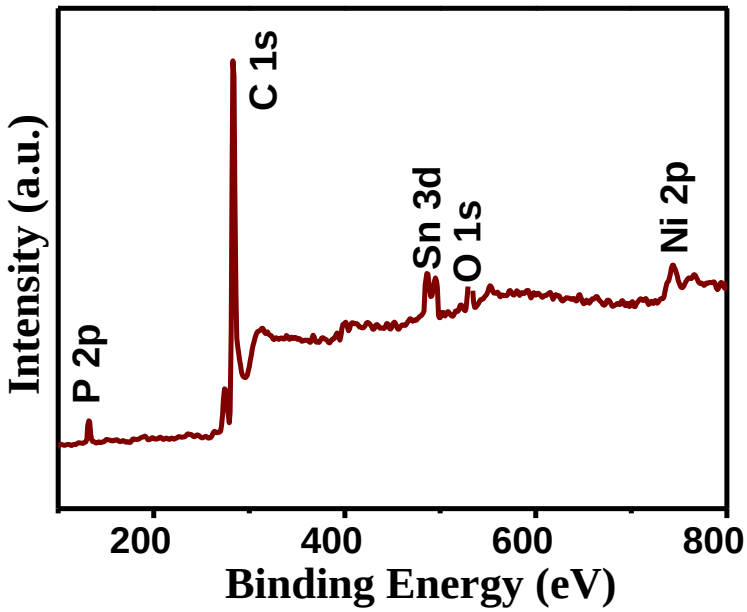

Figure S6. XPS survey spectrum of Ni-Graphene-CNTs-Sn_4P_3 sample refers to the presence of Ni, P, Sn, O and C elements.

In the high-resolution spectra of Ni 2p (Figure S7a) the peak centred at 852.21 and 855.76 eV corresponds to Ni $2p_{3/2}$ of metallic nickel (Ni^0) and Ni in the form of oxide (Ni-O).[1,2] The higher binding energy Ni $2p_{1/2}$ peak centred at 873.15 eV corresponds to nickel hydroxide (Ni(OH_2)) formation.[2] These peaks are accompanied by two other satellite peaks of Ni $2p_{1/2}$ at 861.36 eV and 864.1 eV indicating the presence of Ni in the form of oxide/hydroxide.[2] In C1s spectra (Figure S7b) the formation of C-C, C-O-C, and O-C=O bonds have been verified by the peaks centred at 284.89, 286.65, 289.10 eV, respectively.[3,4] The presence of C-O-C, and O-C=O bonds may be related to the induced defect state of the carbonaceous matrix during the growth process (as discussed in the Raman analysis).[3] Figure S7c shows the core-level spectra of Sn 3d where the two peaks at 487.28 eV and 495.40 eV can be assigned to Sn $3d_{5/2}$ and Sn $3d_{3/2}$ of Sn_4P_3, respectively.[5–7] These two peaks have been shifted by approximately 0.7 eV as compared to the reported Sn_4P_3, which indicates that the Sn centre is in rich in electron density due to backflow of electron density from carbon matrix to Sn centre in the heterostructure.[8–10] Further, in high-resolution spectra of P 2p (Figure S7d), peak at 128.51 eV represents the P $2p_{3/2}$ bonding. Another peak at around 133.40 eV is ascribed to the surface oxidation of Sn_4P_3 and may be attributed to the possible P-O-C/P-O bond formation.[6,11] The formation of such phosphate bonds not only helps in anchoring the electrolyte on the catalyst surface as well as promotes the proton-coupled electron transfer process (PCET) for OER activity.[4,12,13] Conclusively, the XPS analysis reveals a strong

electronic interaction between Sn_4P_3 and carbonaceous matrix *via* synergetic effect for boosting the electrochemical performance of the heterostructure.[3]

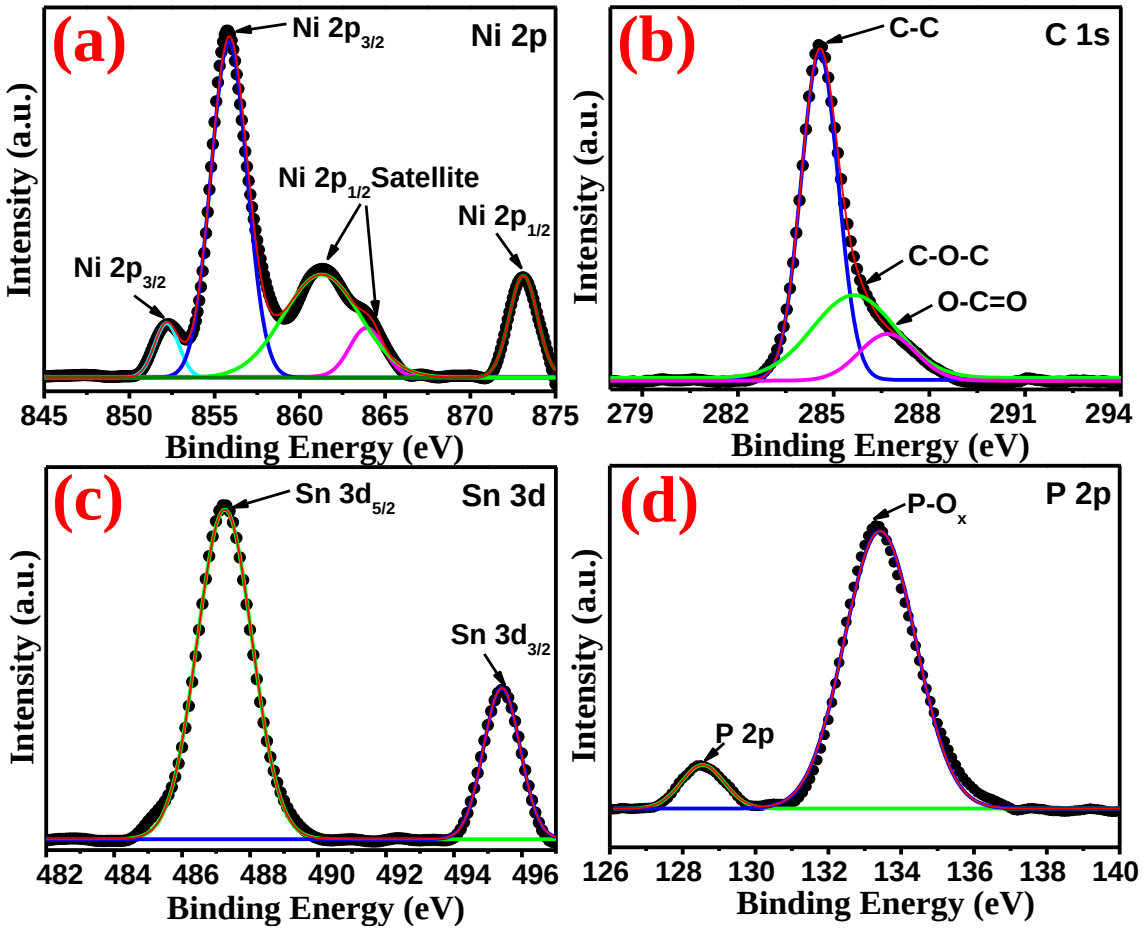

Figure S7. High-resolution XPS spectra of (a) Ni 2p, (b) C 1s, (c) Sn 3d (d) P 2p in Ni-Gr-CNTs-Sn_4P_3 heterostructure.

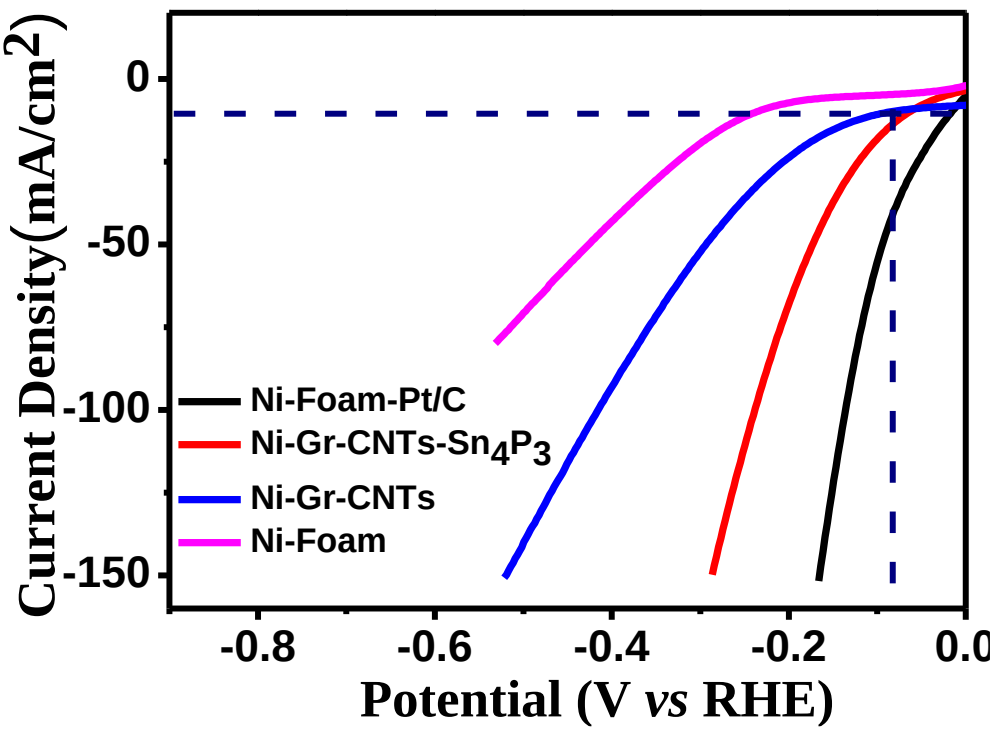

Figure S8. LSV polarization curves of as-designed Ni-Pt/C, Ni-Gr-CNTs-Sn_4P_3, Ni-Gr-CNTs, and Ni-foam electrodes in 0.5M H_2SO_4 electrolyte solution (zoomed-in portion of Figure 4a till 150 mA/cm^2 current density), which indicates the significant reduction of overpotential after the decoration of Sn_4P_3 on carbon matrix.

Table S1. Comparison of the overpotential values (for HER) at different current densities for all the as-grown samples in 0.5M H_2SO_4 solution.

Samples	Over Potential (mV) @10 mA/cm^2	Over Potential (mV) @50 mA/cm^2	Over Potential (mV) @100 mA/cm^2
Ni-Pt/C	15	94	136
Ni-Gr-CNTs-Sn_4P_3	**62**	**172**	**239**
Ni-Gr-CNTs	96	293	415
Ni-foam	237	425	-

Table S2. The catalytic HER performance of the as-designed Ni-Gr-CNTs-Sn_4P_3 electrode in comparison with the recent development of monometallic phosphides.

S.No.	Catalysts	Medium	Current Density (mA/cm^2)	Overpotential (mV)	Tafel Slope (mV/dec)	Ref
1	CoP/CFP	0.5 M H_2SO_4	10 20 100	128.1 144.4 190.8	49.7	[14]
2	Co_2P@C/CC	0.5 M H_2SO_4	10 100	103 179	40.8	[15]
3	Ni_2P NPs/CC	0.5 M H_2SO_4 1 M KOH	10 10	69 73	55 73	[16]
4	FeP/VAGNs/CC	0.5 M H_2SO_4	10	53	42	[17]
5	CoP/CC	0.5 M H_2SO_4	10 20 100	67 100 204	51	[18]
6	Cu_3P NW/CF	0.5 M H_2SO_4	1 10 100	79 143 276	67	[19]
7	WP_2 NS/CC	1.0 M PBS 1.0 M KOH	10 10	261 167	98 81	[20]
8	Cu_3P/NF	1 M KOH	10	115	62	[21]
9	FeP NAs/CC	0.5 M H_2SO_4	1 10	113 202	45	[22]
10	Ni_2P-G/NF	0.5 M H_2SO_4	5	50	51	[23]
11	CoP/Ti	0.5 M H_2SO_4	10 100	90 146	43	[24]
12	MoP_2 NPs/Mo	0.5 M H_2SO_4 1.0 M PBS 1 M KOH	10	143 211 194	57 81 80	[25]
13	Ni_2P-G@NF	0.5 M H_2SO_4 1 M KPi 1 M KOH	10 2 10	105 40 50	38 40 30	[26]
14	CoP_3/NAs	0.5 M H_2SO_4	10 100	65 137	46	[27]
15	Ni_2P/rGO/NF	0.5 M H_2SO_4	10	115	100	[28]
16	$Ni_{12}P_5$ NPs	0.5 M H_2SO_4	20	143	63	[29]
17	Ni_2P NPs	0.5 M H_2SO_4	20	130	46	[30]

18	CoP/Ti foil	0.5 M H_2SO_4	20	85	50	[31]
19	MoP_2 NS/CC	0.5 M H_2SO_4	10	58	63.6	[32]
20	CoP/rGO	0.5 M H_2SO_4	10	105	50	[33]
21	CoP/CNT	0.5 M H_2SO_4	2 10	70 122	54	[34]
22	Mo_3P	0.5 M H_2SO_4			92	[35]
23	Cuf@Ni_5P_4	0.5 M H_2SO_4	10	90	49	[36]
24	NiP_2/CNFs	0.5 M H_2SO_4	10	71	74	[37]
25	MOF Derived porous Ni_2P NS	1 M KOH	10	168	63	[38]
26	MOF Derived Ni_2P polyhedron	0.5 M H_2SO_4	10	310	73	[39]
27	Ni_2P/Ni/NF	1 M KOH	10 20	98 120	72	[40]
28	Ni_5P_4 on Nickel foil	0.5 M H_2SO_4	10	140	40	[41]
29	FeP NA/Ti	0.5 M H_2SO_4	10 20 100	55 72 127	38	[42]
30	Co-PP/Au	0.5 M H_2SO_4	10	183	59	[43]
31	Ni_2P@NSG	0.5 M H_2SO_4	10	110	43	[44]
32	**Ni-Gr-CNTs-Sn_4P_3**	**0.5 M H_2SO_4**	**10**	**62**	**56**	**This Work**

CFP- carbon fiber paper, CC-carbon cloth, NPs-nanoparticles, VAGNs- vertical aligned graphene nanosheets, NWs-nanowire arrays, CF-carbon fiber, NS-nanosheet arrays, NF- nickel foam, NAs- nanorod arrays, G/NF-3D graphene-nickel foam, Cuf-copper foam

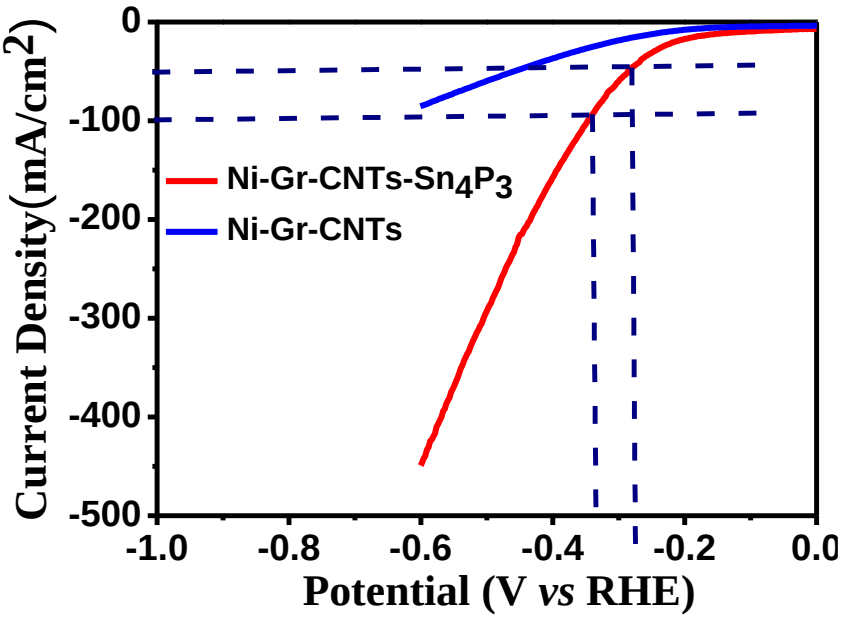

Figure S9. LSV polarization curves corresponding to Ni-Gr-CNTs-Sn_4P_3 and Ni-Gr-CNTs electrodes in 1M KOH solution.

Tafel plot:

To calculate the value of the Tafel slope, the linear region of the Tafel plot is fitted using the Tafel formula: ŋ = b log (J) + a, where ŋ refers to overpotential, J refers to current density, b refers to the Tafel slope and a is constant. b= 2.3RT/αF (R-gas constant, T- absolute temperature, α-symmetry coefficient, F-faraday constant). Faster charge transfer in the electrochemical process can be predicted by the lower value of the Tafel slope (b).[3]

Hydrogen evolution reaction mechanism:

There are two different reaction mechanisms involved in the Hydrogen evolution reaction under acid and alkaline medium proceed *via* three steps. One of the mechanisms is Volmer-Heyrovsky and another is Volmer-Tafel, in which the primary discharge step *i.e.*, Volmer is common in both the mechanism.[3]

Under acidic medium:

(1) $H_3O^+ + e^- + A \rightleftharpoons A\text{-}H_{ads} + H_2O$; Volmer reaction (discharge Step).

Here, electrons are transferred to the surface of the cathode and simultaneously hydronium ions (H_3O^+) are coming from the electrolyte to form A-H_{ads} intermediate state (A denotes the active site of the catalyst). Here, b ~ 120 mV.

(2) A-H_{ads} + H_3O^+ + e^- ⇌ H_2 + A + H_2O; Heyrovsky reaction (desorption step). In this case, when the density of H_{ads} on the active catalyst surface is low then H_{ads} intermediates combine with the new electron and hydronium ions and produced H_2 molecule; b~ 40 mV.

(3) A-H_{ads} + H_{ads} -A ⇌ H_2 + 2A; Tafel reaction (Recombination Step). Whenever the density of H_{ads} on the active catalyst surface is high then the two adjacent H_{ads} intermediates combine and generate H_2 molecule. b~ 30 mV.

Under alkaline medium:

(1) $H_2O + e^- + A \rightleftharpoons A\text{-}H_{ads} + OH^-$; Volmer-discharge Step

(2) $H_2O + e^- + A\text{-}H_{ads} \rightleftharpoons A + H_2 + OH^-$; Heyrovsky-desorption step

(3) A- H_{ads} + H_{ads}-A ⇌ H_2 + 2A; Tafel-recombination Step

The slowest step i.e., the rate-determining step is dependent on the affinity between intermediates and the active catalyst surface. The reaction will be dominated by the Volmer step if the bonding between the active catalyst site and hydrogen intermediate is weak. However, if the bonding strength between the active catalyst site and hydrogen intermediates is very strong then the Heyrovsky or Tafel would be the rate-limiting dominating step.[3,45] To facilitate the adsorption and desorption process for the efficient production of H_2 molecule, it is necessary to get moderate bonding between the active catalyst site and hydrogen intermediate.[45]

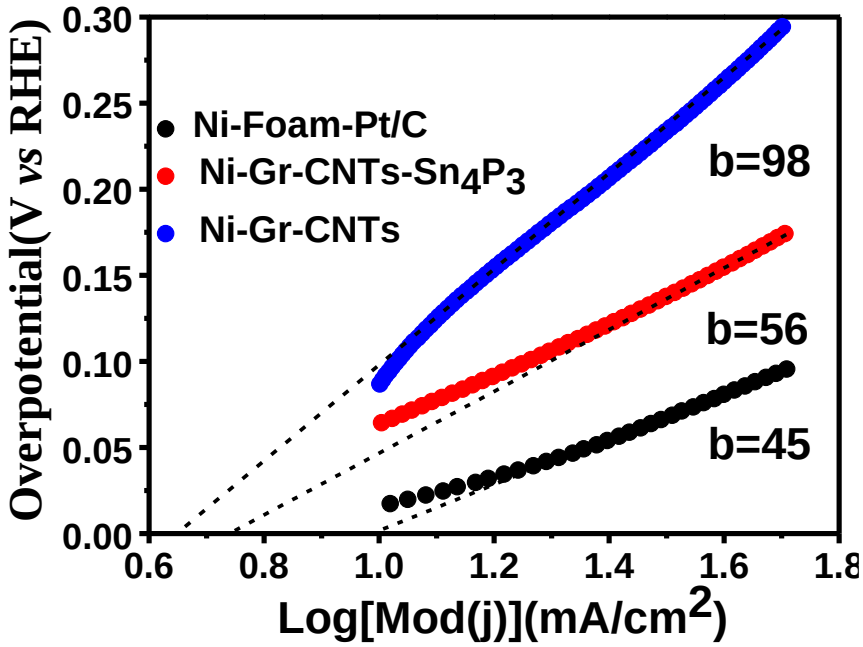

Figure S10. Calculated exchange current density from the extrapolation of Tafel slope at an overpotential of 0 V has been found to be 10, 5.6, and 4.4 mA/cm^2 for Ni-Pt/C, Ni-Gr-CNTs-Sn_4P_3 and Ni-Gr-CNTs electrodes, respectively. Higher the value of exchange current density leads to faster rate of HER kinetics.

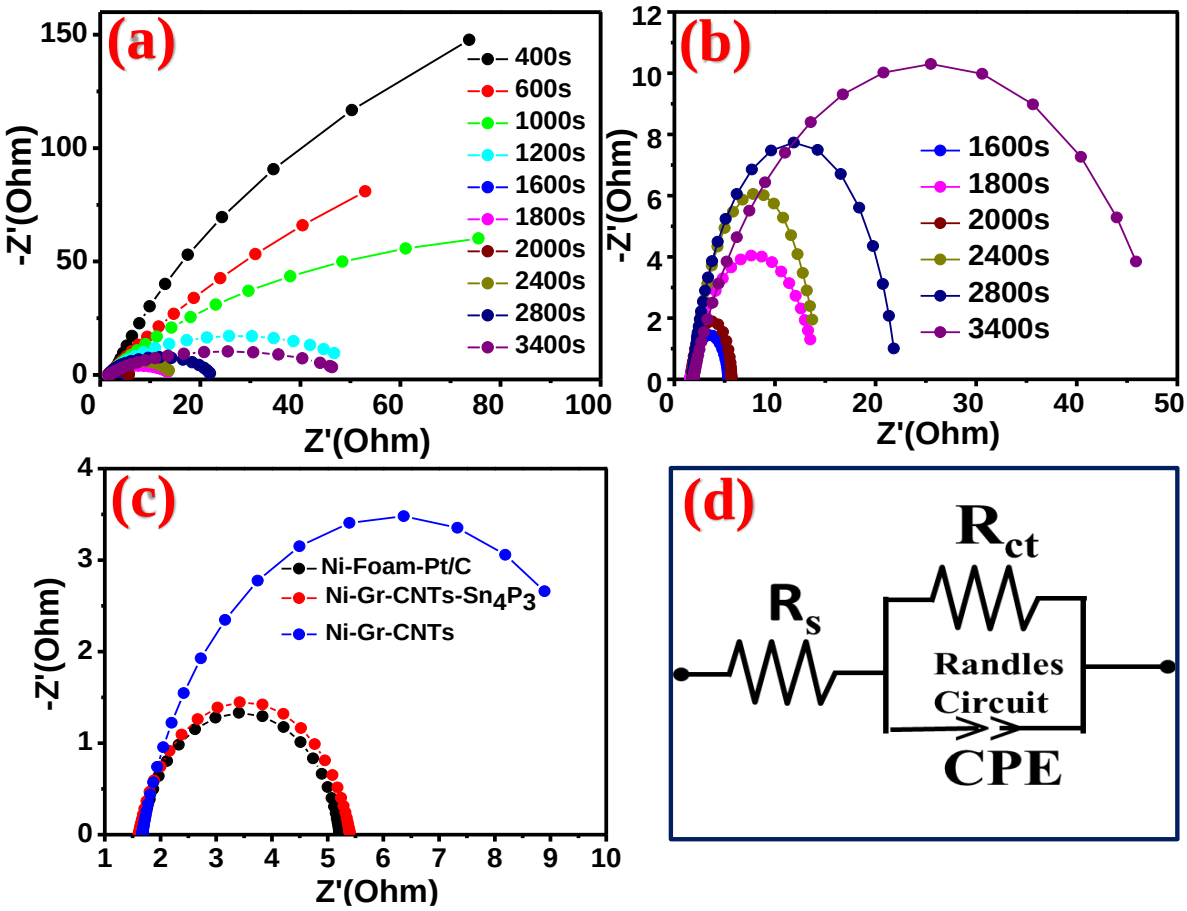

Figure S11. Electrochemical impedance spectra (EIS) analysis. Nyquist plots of (a) Ni-Gr-CNTs-Sn_4P_3 with different deposition times (400-3400s) of Sn (b) shows the zoomed-in portion for the deposition time of 1600, 1800, 2000, 2400, 2800 and 3400s. The lowest R_s and R_{ct} values have been found for the Sn-1600s deposition sample as compared to the others which lead to the best electrocatalytic activity; (c) Ni-Pt/C, Ni-Gr-CNTs-Sn_4P_3 and Ni-Gr-CNTs. (d) shows the equivalent circuit diagram to fit all the EIS data. The EIS is tested in a three-electrode system over a frequency range from 100 kHz to 0.01 Hz with an AC amplitude of 10 mV at a constant voltage of -300 mV (*vs* RHE) in 0.5M H_2SO_4 solution. The R_s and R_{ct} values of the Ni-Gr-CNTs-Sn_4P_3 and Ni-Pt/C are very close to each other indicating a high charge transfer process.

Table S3. Comparison of series (R_s) and charge transfer resistance (R_{ct}) of Ni-Gr-CNTs-Sn_4P_3 with the different deposition times of Sn where the Sn-1600s shows the lowest resistance values.

Ni-Gr-CNTs-Sn_4P_3 with different Sn deposition time	Series Resistance (R_s) Ohm	Charge transfer Resistance (R_{ct}) Ohm
400 s	2.16	480
600 s	1.77	356
1000 s	1.67	196
1200 s	1.61	12.7
1600 s	1.55	3.79
1800 s	1.62	4.92

2000 s	1.78	3.91
2400 s	1.80	9.3
2800 s	1.82	16.3
3400 s	1.87	33.2

Table S4. Comparison of series (R_s) and charge transfer resistance (R_{ct}) of the as-prepared samples in 0.5M H_2SO_4 solution.

Samples	Series Resistance (R_s) Ohm	Charge transfer Resistance (R_{ct}) Ohm
Ni-Foam-Pt/C	1.61	3.51
Ni-Gr-CNTs-Sn_4P_3	1.55	3.79
Ni-Gr-CNTs	1.67	11.12

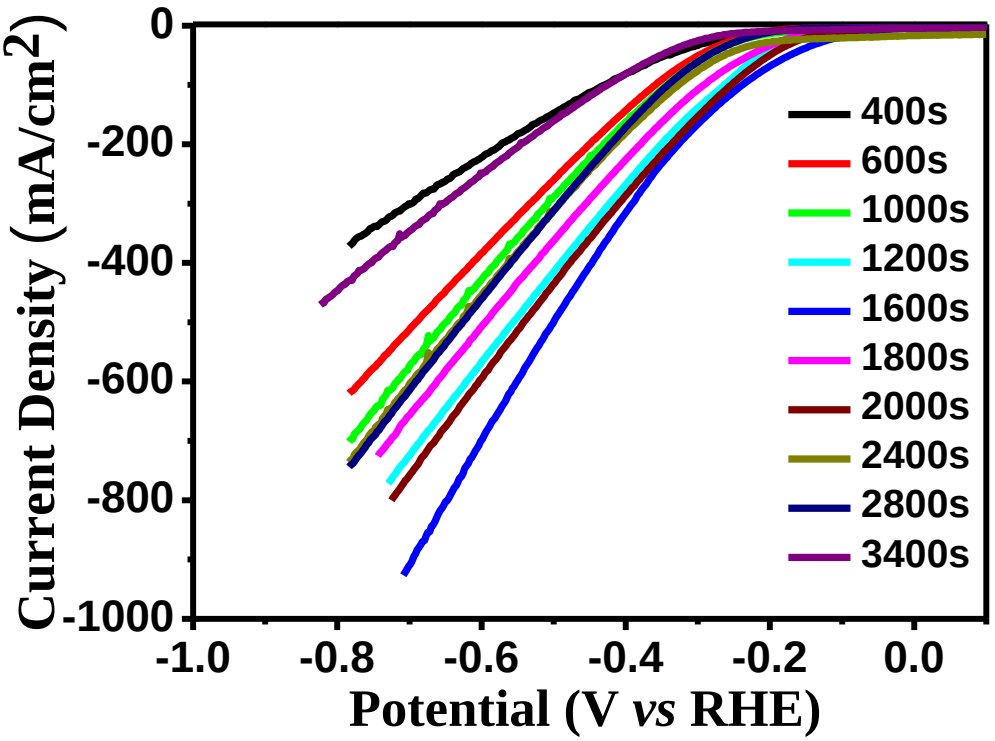

Figure S12. HER LSV polarization curves of Ni-Gr-CNTs-Sn_4P_3 at different deposition times of Sn in 0.5M H_2SO_4. The best performance has been achieved from the sample where the deposition of Sn is 1600s.

Table S5. Summary of overpotential at a different current density of HER (0.5M H_2SO_4) for Ni-Gr-CNTs-Sn_4P_3 with the different deposition time of Sn.

Sn deposition time	Over Potential (mV) @10 mA/cm^2	Over Potential (mV) @50 mA/cm^2	Over Potential (mV) @100 mA/cm^2
400 s	176	342	428
600 s	203	298	359
1000 s	169	286	343
1200 s	90	213	263
1600 s	62	172	239
1800 s	137	227	291
2000 s	103	201	251
2400 s	164	262	327
2800 s	193	285	340
3400 s	209	350	424

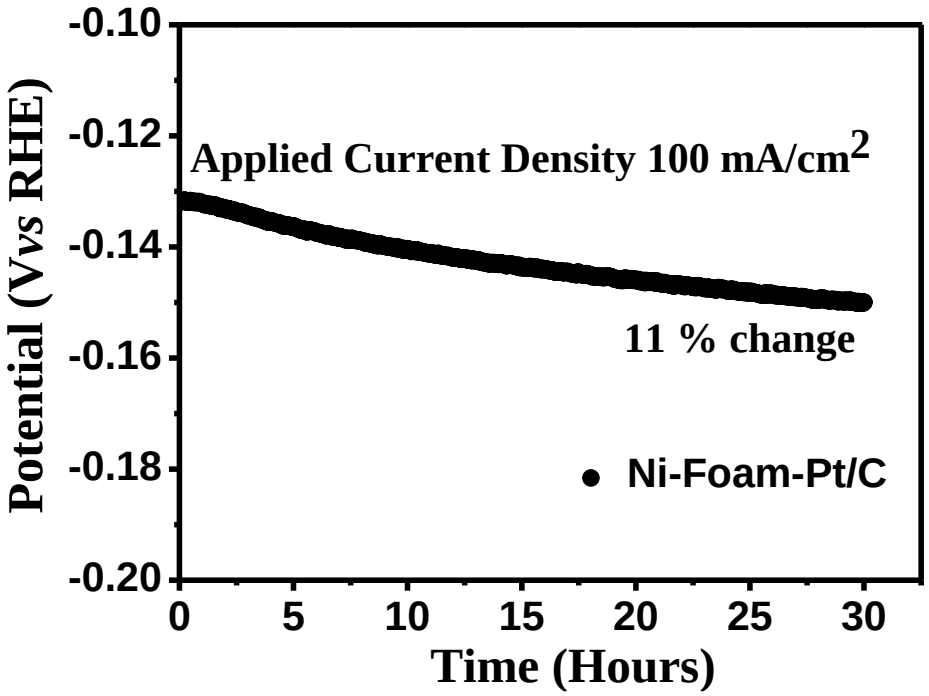

Figure S13. Chronopotentiometric analysis of the stability test at least for 30 hours with ~11% change of potential for Ni-foam-Pt/C at constant applied current density of 100 mA/cm^2.

Electrochemically Active Surface Area (ECSA) and Roughness factor (RF) calculation

To estimate ECSA, the double-layer capacitance (C_{dl}) is calculated by carrying out cyclic voltammetry (CV) curves in the non-faradaic region at a different scan rate of 10 to 100 mV/s in 0.5M H_2SO_4 and 1M KOH solution. The capacitive current density (ΔJ) can be determined by the product of the scan rate (v) and the double-layer capacitance[46]

$\Delta J = v\, C_{dl}$

The scan rates are fitted with the capacitive current density differences ($\Delta J = |j_a - j_c|$) and from the slope, the C_{dl} value has been estimated. The C_{dl} values of Ni-Gr-CNTs-Sn_4P_3 is found to be 21 mF/cm^2 and 19.5 mF/cm^2 for HER and OER, respectively.

The ECSA can be calculated by dividing C_{dl} with the specific capacitance (C_{sp}) of the surface of the electrode or the capacitance of an atomically smooth planar surface of the material per unit area under identical electrolyte condition[46]

$$ECSA = C_{dl} / \{C_{sp} \text{ per ECSA cm}^2\}$$

The commonly used C_{sp} value for a flat metal surface is varying between 0.02-0.06 mF/cm^2 and here 0.04 mF/cm^2 value has been consider but it should be noted that the C_{sp} value of such kind of Sn_4P_3 along with graphene-CNTs is not available, and thus the choice of 0.04 mF/cm^2 may create some errors.[2,3,11,47] The ECSA value of Ni-Gr-CNTs-Sn_4P_3 is calculated to be 525 and 487 cm^2 for HER and OER, respectively.

The roughness factor (RF) is also calculated by using the following formula.[48]

RF = Catalyst active surface area (ECSA)/Geometric surface area

The geometric surface area of the electrode is considered to be (1x1.2) cm^2 shown in Figure S28. The RF value of Ni-Gr-CNTs-Sn_4P_3 is calculated to be 437 and 406 for HER and OER, respectively.

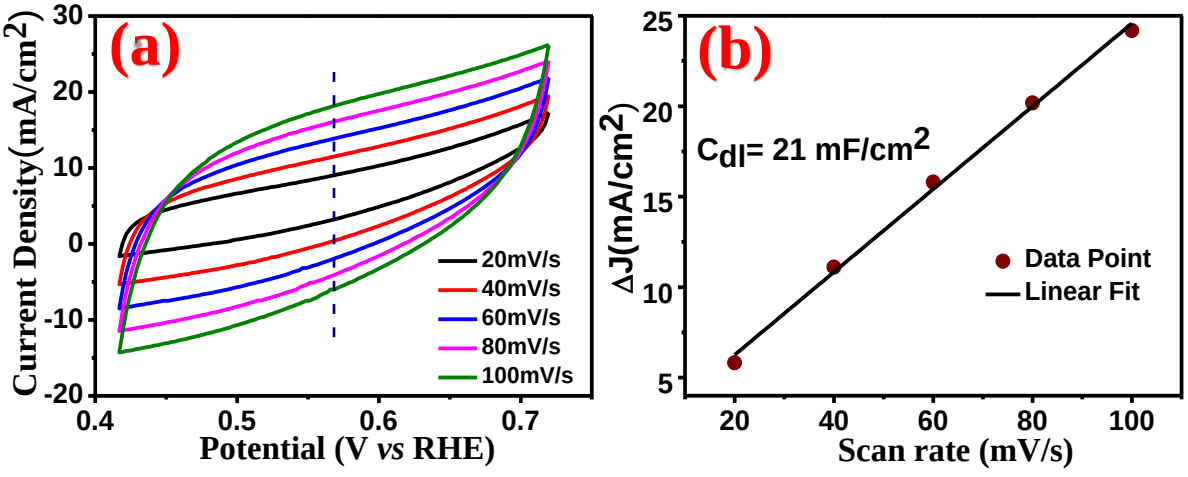

Figure S14. (a) Cyclic voltammograms of Ni-Gr-CNTs-Sn_4P_3 in the non-faradic region of 0.41 to 0.71 V (*vs* RHE) at different scan rates ranging from 20 mV/s to 100 mV/s with an interval of 20 mV/s in 0.5M H_2SO_4 and corresponding (b) capacitive currents density difference (ΔJ) as a function of scan rate has been plotted at 0.56 V (*vs* RHE) and the slope (C_{dl}) calculated from the linear fitting has been found to be 21 mF/cm^2. The estimated values of the C_{dl} indicate the significantly higher electro-active surface area of Ni-Gr-CNTs-Sn_4P_3.

Active site density (n) and Turn-over frequency (TOF) calculations

The active site density (n) is defined as the following formula[49,50]:

n=Q/2F in HER process.

n=Q/4F in OER process.

Where Q is the voltammetric charge and F is the Faraday constant (F) ~ 96485 C/mol

The CV analysis has been carried out within a potential window of -0.2 V to 0.8 V (*vs* RHE) with a scan rate of 50 mV/s in 1M Phosphate buffer Saline shown in Figure S13 for the calculation of the voltammetric charge. The active site density of Ni-Gr-CNTs and Ni-Gr-CNTs-Sn_4P_3 are found to be 2.27x10^{-4} mol/cm^2 and 5.33x10^{-4} mol/cm^2 for HER and 1.13x10^{-4} mol/cm^2 and 2.66x10^{-4} mol/cm^2 for OER, respectively. Here, we consider all the active surface sites include Ni, Sn, P, C atom involved in the HER and OER activity.

Turn-over frequency (TOF) has been calculated using these active site densities (n) and it is given as[49,50]:

TOF = I /2nF for HER process

TOF = I /4nF for OER process

where, I is the current density measured by the LSV plots in HER and OER processes.

The TOF of Ni-Gr-CNTs are 1s^{-1}, 2s^{-1} at overpotentials of 301 mV and 427 mV and 264 mV and 362 mV for Ni-Gr-CNTs-Sn_4P_3 respectively in case of HER. Similarly, for OER the TOF of Ni-Gr-CNTs is calculated to be 0.5s^{-1}@340 mV, 1s^{-1}@400 mV but in the case of Ni-Gr-CNTs-Sn_4P_3, the TOF is achieved to be 0.5s^{-1}@310 mV, 1s^{-1}@410 mV.

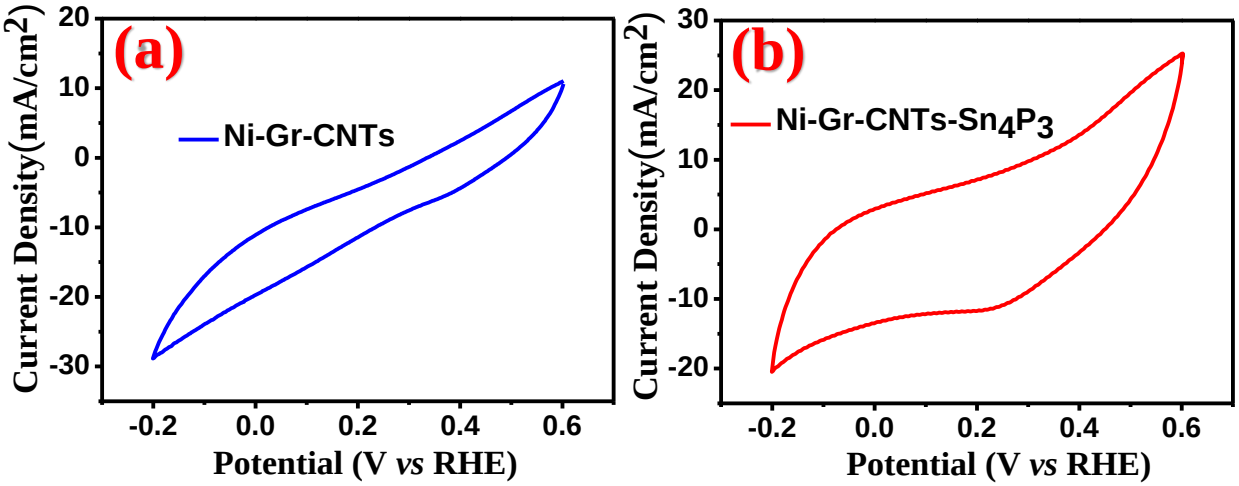

Figure S15. Cyclic voltammograms of (a) Ni-Gr-CNTs and (b) Ni-Gr-CNTs-Sn_4P_3 in 1M PBS (pH ~ 7) solution under the potential range between -0.2 V (*vs* RHE) to 0.6 V (*vs* RHE) at a scan rate of 50 mV/s helps to calculate the active site density and TOF.

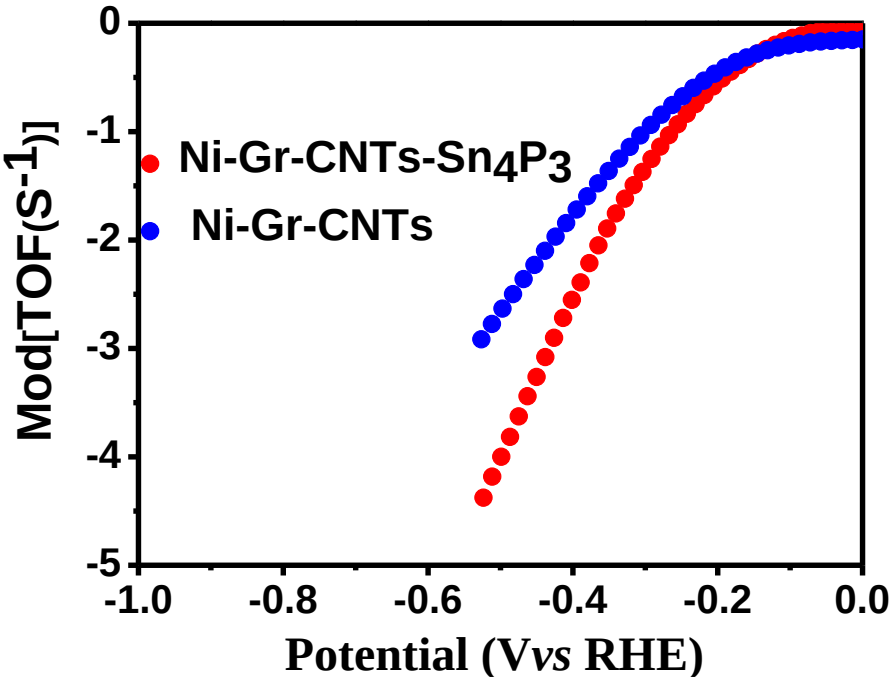

Figure S16. The TOF values have been calculated for Ni-Gr-CNTs-Sn_4P_3 ($1s^{-1}$@264 mV, $2s^{-1}$@362 mV) and Ni-Gr-CNTs ($1s^{-1}$@301 mV, $2s^{-1}$@ 427 mV); where the high TOF achieved at low applied potential indicates the good electrocatalytic activity of Ni-Gr-CNTs-Sn_4P_3 towards water splitting.

Table S6. OER catalytic performance of Ni-Gr-CNTs-Sn_4P_3 in comparison with the recently developed monometallic phosphide-based catalysts.

S.No.	Catalysts	Medium	Current Density (mA/cm^2)	Overpotential (mV)	Tafel Slope (mV/dec)	Ref
1	Co_2P NN	1 M KOH	10	310	50	51
2	CoP NR	1 M KOH	10	340	71	52
3	CoP/C	1 M KOH	10	360	66	53
4	Ni_2P NWs	1 M KOH	10	400	60	54
5	Ni_2P NPs	1 M KOH	10	500	70	55
6	Co-P foam	1 M KOH	10	131	74	56
7	Ni_5P_4-NF	1 M KOH	10	290	40	41
8	Ni-P/CP	1 M KOH	10	190	73	57
9	CoP NR/NF	1 M KOH	10	390	65	58
10	Co-P film	1 M KOH	10	345	47	59
11	CoP NWs	1 M KOH	10	248	78	60
12	Co-P/NC	1 M KOH	10	354	52	61
13	Co_2P/CoNPC	1 M KOH	10	328	78	62
14	Co_2P NCs	1 M KOH	10	280	60.4	63
15	$Ni_{12}P_5$/NF	1M KOH	10	240	225	64
16	NiP_2/CC	1 M KOH	20	310	107.8	65
17	MOF-Ni_2P NS	1 M KOH	10	320	105	38
18	Co-PP/Au	1 M KOH	10	340	-	43
19	$Ni_{12}P_5$ - O-WCNT	1 M KOH	10	280	62	66
20	Au/$Ni_{12}P_5$ NPs	1 M KOH	10	340	49	67
21	Ni_2P@NSG	1 M KOH	10	240	43	44
22	Ni_2P	1 M KOH	10	280	115	68
23	FeP@Au	1 M KOH	10	320	56.8	69
24	Ni_2P@C/G	1 M KOH	10	285	44	70
25	Multishelled Ni_2P	1 M KOH	10	270	40.4	71
26	CoP-CNT	1M NaOH	10	330	50	72
27	C@Ni_8P_3	1 M KOH	10	144	51	73
28	CoP_3 NAs/CFP	1 M KOH	10	334	62	27
29	CoP_2/RGO	1 M KOH	10	300	96	74
30	Cuf@Ni_5P_4	1 M KOH	20	210	127	36
31	**Ni-Gr-CNTs-Sn_4P_3**	**1 MKOH**	**20**	**169**	**88**	**This wor**

						k

NN-nanoneedles, NR-nanoroad, C-carbon support, NWs-nanowire arrays, NPs-nanoparticles, CFP/CP- carbon fiber paper, NC-nanopolyhedrons composed, CoNPC- Co, N, P doped carbon, NCs- nanocrystals, NF- nickel foam, CC-Carbon Cloth, NS-nanosheet, Co-PP- cobalt phosphide phosphate films, O-WCNT-oxidized multiwall carbon nanotube, NSG- N-and S-doped graphene, C/G-carbon confined graphene, NAs- nanorod arrays

Table S7. The OER overpotential values at different current densities for all as-prepared samples in 1 M KOH solution.

Samples	Over Potential (mV) @20 mA/cm^2	Over Potential (mV) @50 mA/cm^2	Over Potential (mV) @100 mA/cm^2
Ni-Gr-CNTs-Sn_4P_3	**169**	**289**	**380**
Ni-foam-RuO_2	290	360	450
Ni-Gr-CNTs	320	390	-
Ni-foam	430	-	-

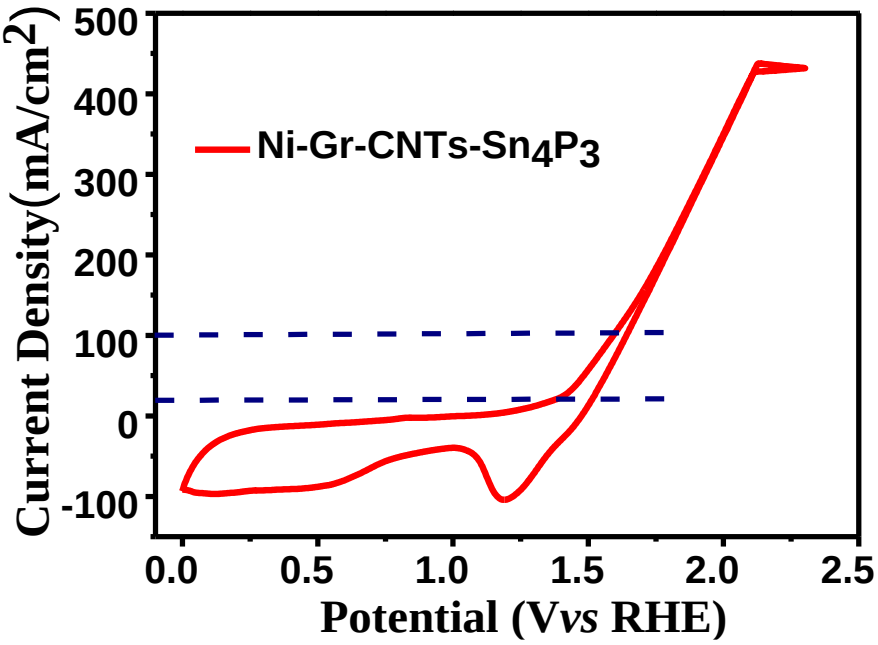

Figure S17. CV analysis of Ni-Gr-CNTs-$Sn_4P_3$with a scan rate of 2 mV/s in the potential range of 0 to 2.25 V (*vs* RHE). It shows a very small oxidation peak at 1.45 V (*vs* RHE) and a prominent reduction peak at 1.19 V (*vs* RHE).

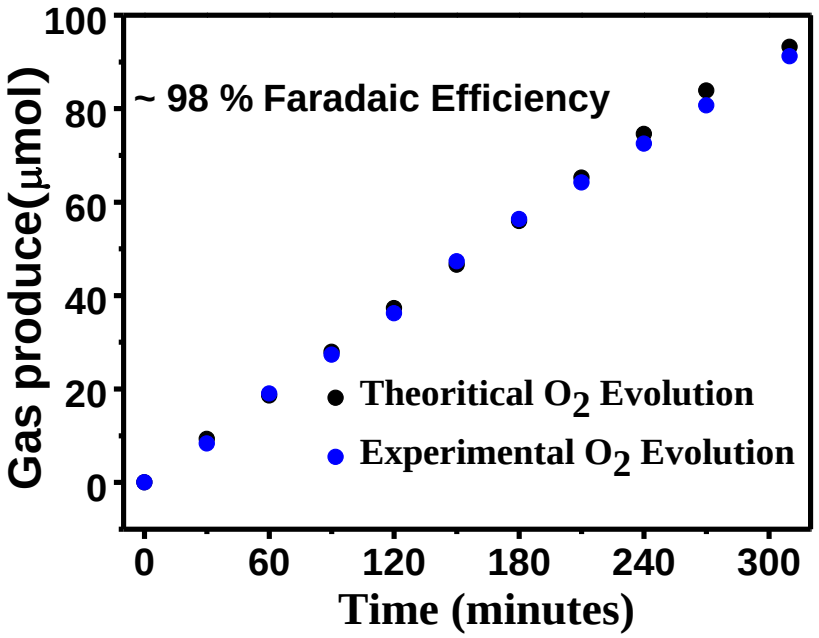

Figure S18. The experimentally and theoretically estimated amount of O_2 produced by the Ni-Gr-CNTs-Sn_4P_3 electrode at a fixed potential of 1.45 V in 1M KOH solution. A very small deviation in experimental and theoretical result indicates ~ 98% faradaic efficiency of O_2 production.

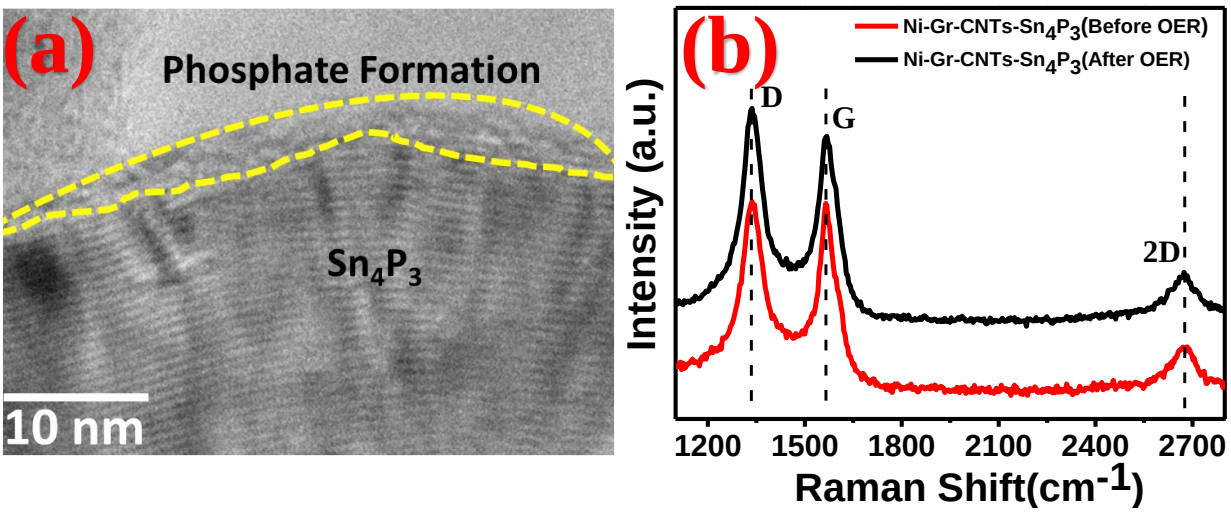

Figure S19. Post OER analysis of Ni-Gr-CNTs-Sn_4P_3 (a) HR-TEM and (b) Raman analysis indicates that surface oxidation of Sn4P3 doesn't imact on template carbon matrix in the Raman response.

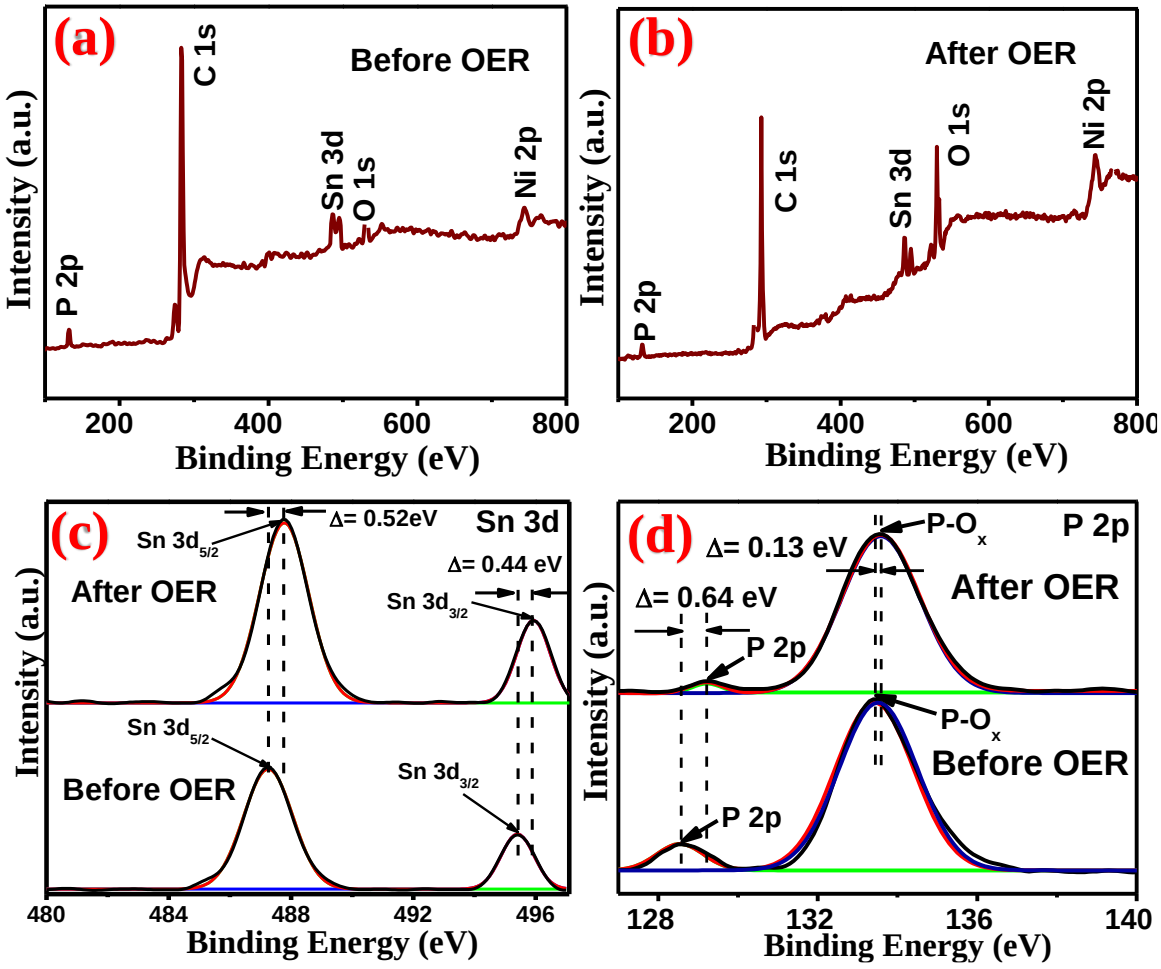

Figure S20. XPS survey spectrum of (a) before and (b) post OER process of Ni-Gr-CNTs-Sn_4P_3. The corresponding XPS high-resolution spectrum of (c) Sn 3d (d) P 2p under before and after OER process indicate that surface oxidation has a prominent impact on XPS response.

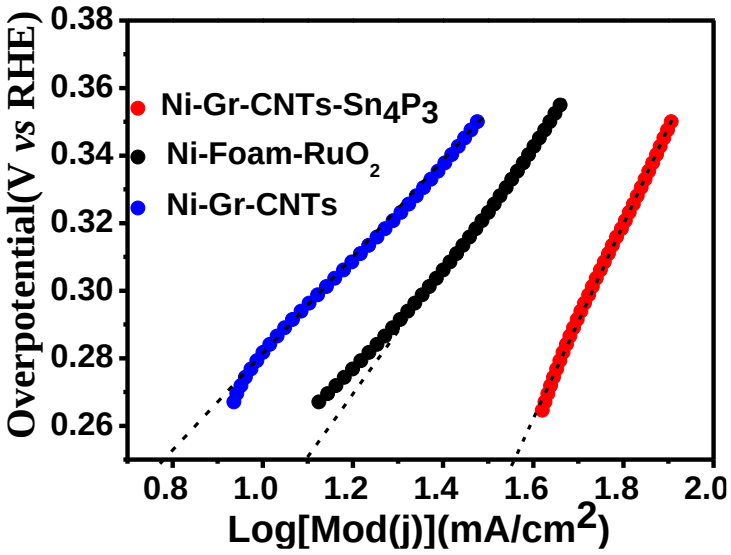

Figure S21. The exchange current density is calculated from the extrapolation of Tafel slope at the overpotential of 0 V. The exchange current density of Ni-Gr-CNTs-Sn_4P_3, Ni-RuO_2, and Ni-Gr-CNTs are calculated to be 4.7, 2.9, and 2.1 mA/cm^2, respectively.

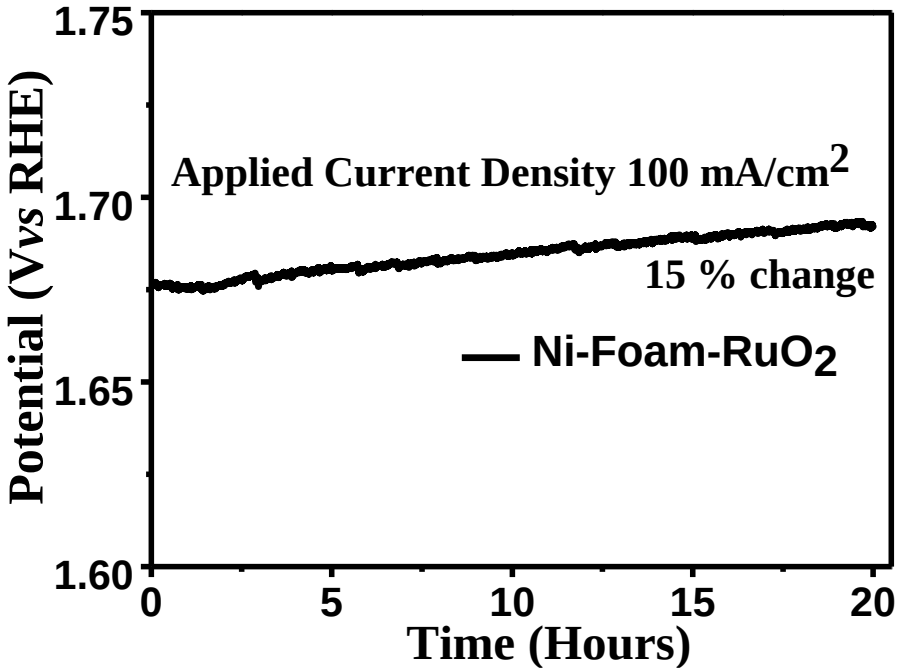

Figure S22. Chronopotentiometric analysis of the stability test at least for 20 hours with ~15% change of potential for Ni-foam-RuO_2 at constant applied current density of 100 mA/cm^2.

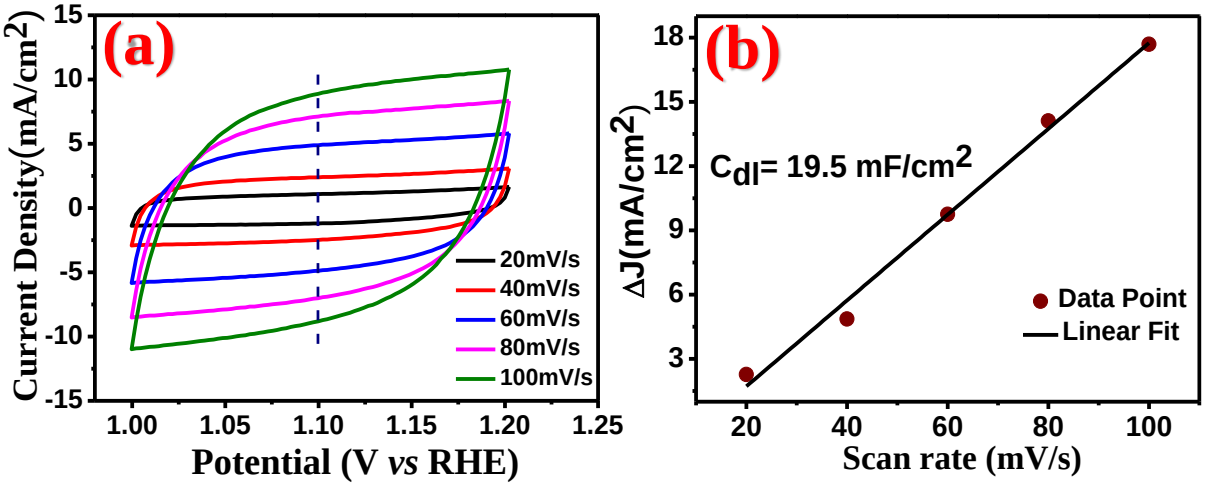

Figure S23. (a) Cyclic voltammograms of Ni-Gr-CNTs-Sn_4P_3 in the non-faradic region of 1 V to 1.2 V (*vs* RHE) at different scan rates ranging from 20 mV/s to 100 mV/s with an interval of 20 mV/s in 1M KOH and corresponding (b) capacitive currents density difference (ΔJ) as a function of scan rate has been plotted at 1.10 V (*vs* RHE) and from the slope, C_{dl} has been calculated to be 19.5 mF/cm^2. The estimated value of the C_{dl} indicates the significantly higher electroactive surface area of Ni-Gr-CNTs-Sn_4P_3 in the OER process.

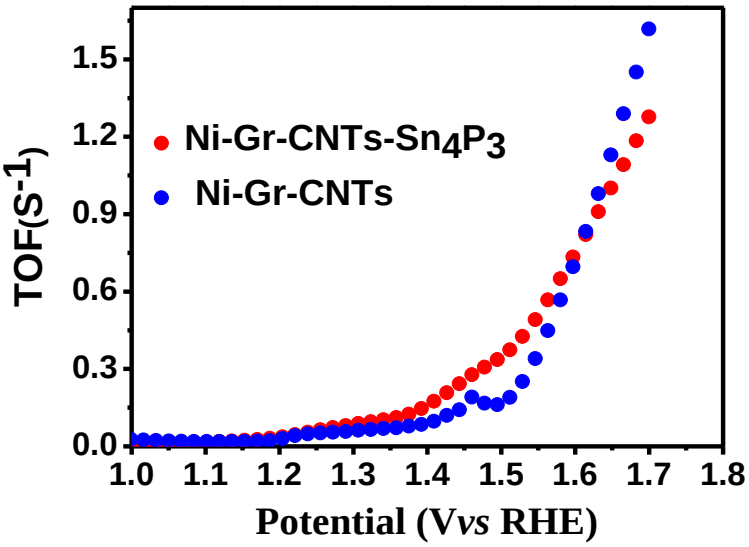

Figure S24. The TOF values of the Ni-Gr-CNTs-Sn_4P_3 ($0.5s^{-1}$@310 mV and $1s^{-1}$@410 mV) and Ni-Gr-CNTs ($0.5s^{-1}$@340 mV and $1s^{-1}$@400 mV) with varying OER potentials; where high TOF achieved at low applied potential indicates the good electrocatalytic activity of Ni-Gr-CNTs-Sn_4P_3 towards water splitting.

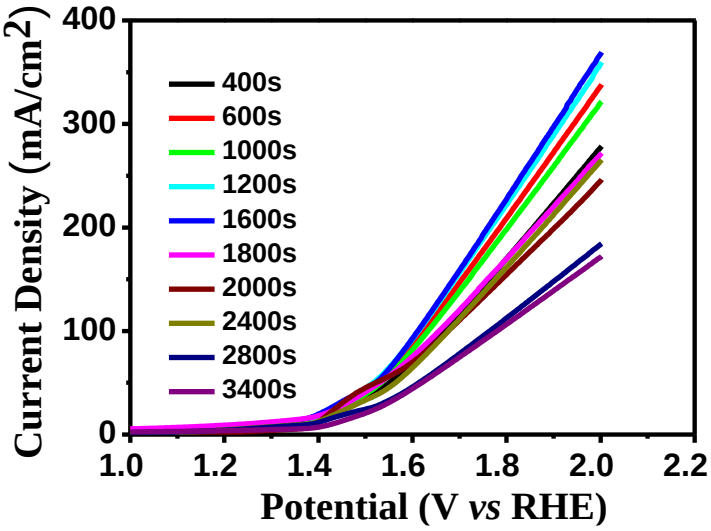

Figure S25. OER LSV polarization curves of Ni-Gr-CNTs-Sn_4P_3 at different deposition times of Sn in 1M KOH.

Table S8. Summary of overpotential values at different current densities for OER (1M KOH) in Ni-Gr-CNTs-Sn_4P_3 with the different deposition times of Sn.

Sn deposition time	Over Potential (mV) @20 mA/cm^2	Over Potential (mV) @50 mA/cm^2	Over Potential (mV) @100 mA/cm^2
400 s	187	320	430
600 s	200	290	390
1000 s	186	300	400
1200 s	178	280	379
1600 s	169	289	375
1800 s	183	299	420
2000 s	193	296	440
2400 s	201	333	446
2800 s	230	382	534
3400 s	265	390	550

Oxygen evolution reaction mechanism:

In alkaline medium, OER involved

$4OH^- \leftrightarrow 2H_2O + O_2 + 4e^-$

The above reaction is followed by four electrons transfer process in several steps.

$A + OH^- \rightarrow A\text{-}OH^* + e^-$;----------$\Delta G_1$

$A\text{-}OH^* + OH^- \rightarrow AO^* + H_2O + e^-$; ----------$\Delta G_2$

$AO^* + OH^- \rightarrow A\text{-}OOH^* + e^-$; ----------$\Delta G_3$

$A\text{-}OOH^* + OH^- \rightarrow AOO^- + H_2O$

$AOO^- \rightarrow A + O_2 + e^-$; ----------$\Delta G_4$

In acid medium, OER is given by:

$2H_2O \leftrightarrow O_2 + 4H^+ + 4e$-

The above reaction proceeds *via* several steps as follows:

$A + H_2O \rightarrow A\text{-}OH^* + H^+ + e$ ----------ΔG_1

$A\text{-}OH^* \rightarrow A\text{-}O^* + H^+ + e^-$; ----------$\Delta G_2$

$A\text{-}O^* + H_2O \rightarrow A\text{-}OOH^* + H^+ + e^-$;----------$\Delta G_2$

$A\text{-}OOH^* \rightarrow A + O_2 + H^+ + e^-$;----------$\Delta G_4$

where A denotes the active metal site on the surface

In acid or alkaline medium, OER takes place *via* generating OH*, O* and OOH* intermediate.

The adsorption energies of the intermediates at different active sites on the catalyst can be determined as:[75,76]

$\Delta E_{OH^*} = E_{OH^*} - E^* - (E_{H2O} - 0.5E_{H2})$

$\Delta E_{O^*} = E_{O^*} - E^* - (E_{H2O} - E_{H2})$

$\Delta E_{OOH^*} = E_{OOH^*} - E^* - (2E_{H2O} - 1.5E_{H2})$

where E* is the energy of the catalytic surface. The adsorption energies in reference to the energy values of H_2O and H_2 molecules in the gas phase i.e., E_{H2O} and E_{H2}, have been calculated from DFT.

Further, the free-energies are calculated as[75,76]

$\Delta G = \Delta E + \Delta ZPE - T\Delta S - \Delta G_U + \Delta G_{pH}$

Here, the small values of zero-point energy (ΔZPE) and entropy change (ΔS), the term ΔZPE and TΔS are neglected and considered to be zero for the simplicity of the calculation. ΔG_U represents the applied electrode potential, that is $\Delta G_U = eU$ and $\Delta G_{pH} = KTln a_{H^+}$ where K as the Boltzmann constant, T is the temperature and a_{H^+} is the pH of the proton. The Gibbs free-energy change for each intermediate reaction is determined at standard conditions (pH= 0, T=298.15 K) as[3,75]

$\Delta G_1 = \Delta G_{OH^*}$

$\Delta G_2 = \Delta G_{O^*} - \Delta G_{OH^*}$

$\Delta G_3 = \Delta G_{O^*} - \Delta G_{OH^*}$

$\Delta G_4 = \Delta G_{O2} - \Delta G_{OOH^*}$

Here, the experimental value of 4.92 eV is considered for ΔG_{O2}.

The theoretical overpotential can be calculated using the given equation:[3]

$\eta^{OER} = \max [\Delta G_1, \Delta G_2, \Delta G_3, \Delta G_4] - 1.23$ eV

Hydrogen evolution reaction involves the H_2 generation at the cathode when the proton gains electron from the catalyst surface. The Gibbs free energy for HER is given as:[3]

$$\Delta G_{H^*} = \Delta E_{H^*} - T\Delta S + \Delta ZPE$$

$$\Delta G_{H^*} = \Delta E_{H^*} + 0.24 \text{ eV}$$

The correction term for adsorption of H-atom i.e., ΔZPE- TΔS is taken as 0.24 eV.

Adhesion energy

Adhesion energy of the heterostructure is given as:[77]

$$E_{adhesion} = \frac{1}{A}\left[E_{Sn_4P_3-SWCNT} - \left(E_{Sn_4P_3} - E_{SWCNT}\right)\right]$$

where $E_{Sn_4P_3-SWCNT}$, $E_{Sn_4P_3}$ and E_{SWCNT} represent the total energies of the heterostructure, Sn_4P_3 and SWCNT, respectively. A is the total surface area (258.97 $Å^2$) of the heterostructure. The XRD analysis represents the most prominent crystalline planes of (107) and (110) for as grown Sn_4P_3 (Figure 3a). Therefore, the free-energies have been computed for OER intermediates on these two different surfaces of Sn_4P_3 as shown in Figure S27. Sn-site is found to be more active as compared to P-site towards OER for both the surfaces and further, Sn-site on (110) surface exhibits the best OER activity. Hence, Sn_4P_3-(110) is chosen to build the heterostructure with metallic SWCNT. The adsorption energies of the OER intermediates (OH*, O* and OOH*) have been computed on Sn as well as P sites (Table S10).

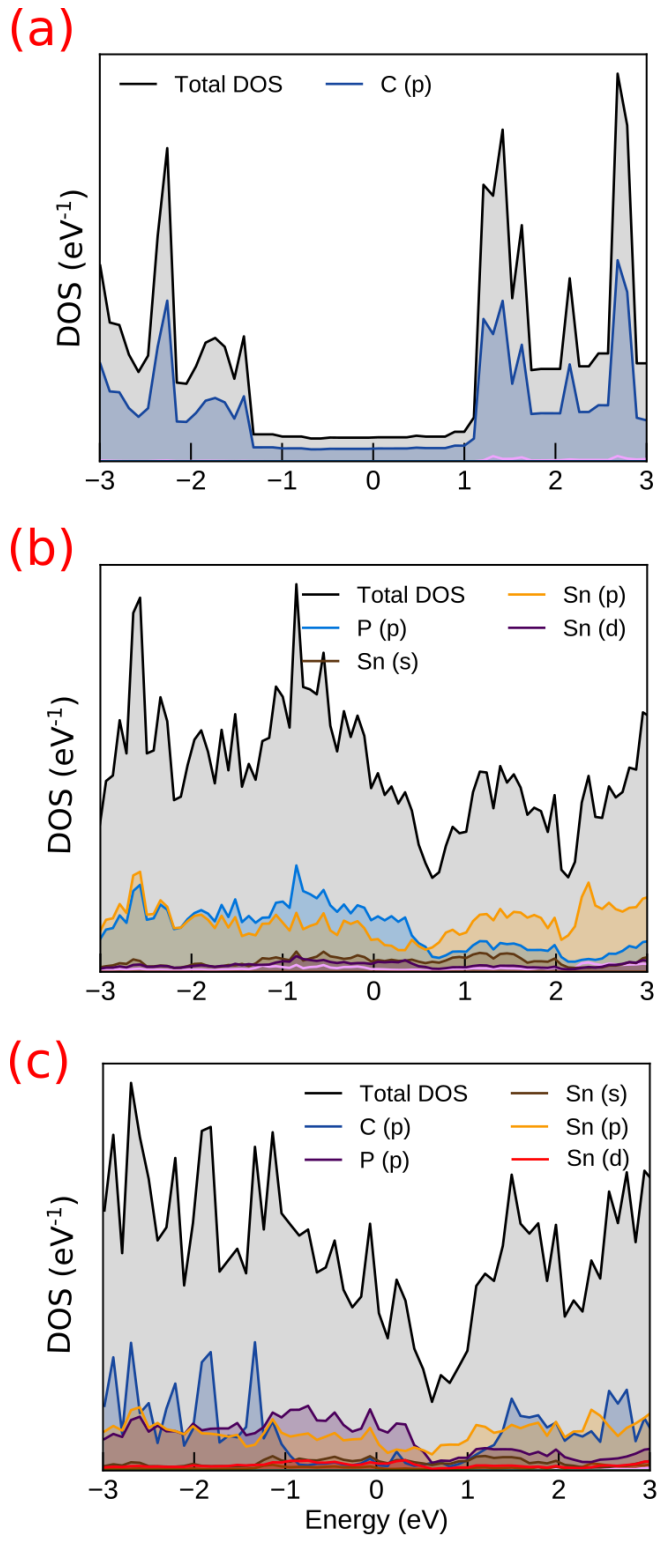

Figure S26. Projected DOS for (a) SWCNT, (b) Sn_4P_3 and (c) Sn_4P_3-SWCNT heterostructure where the higher number of density of states of the heterostructure leads to a faster charge transfer process.

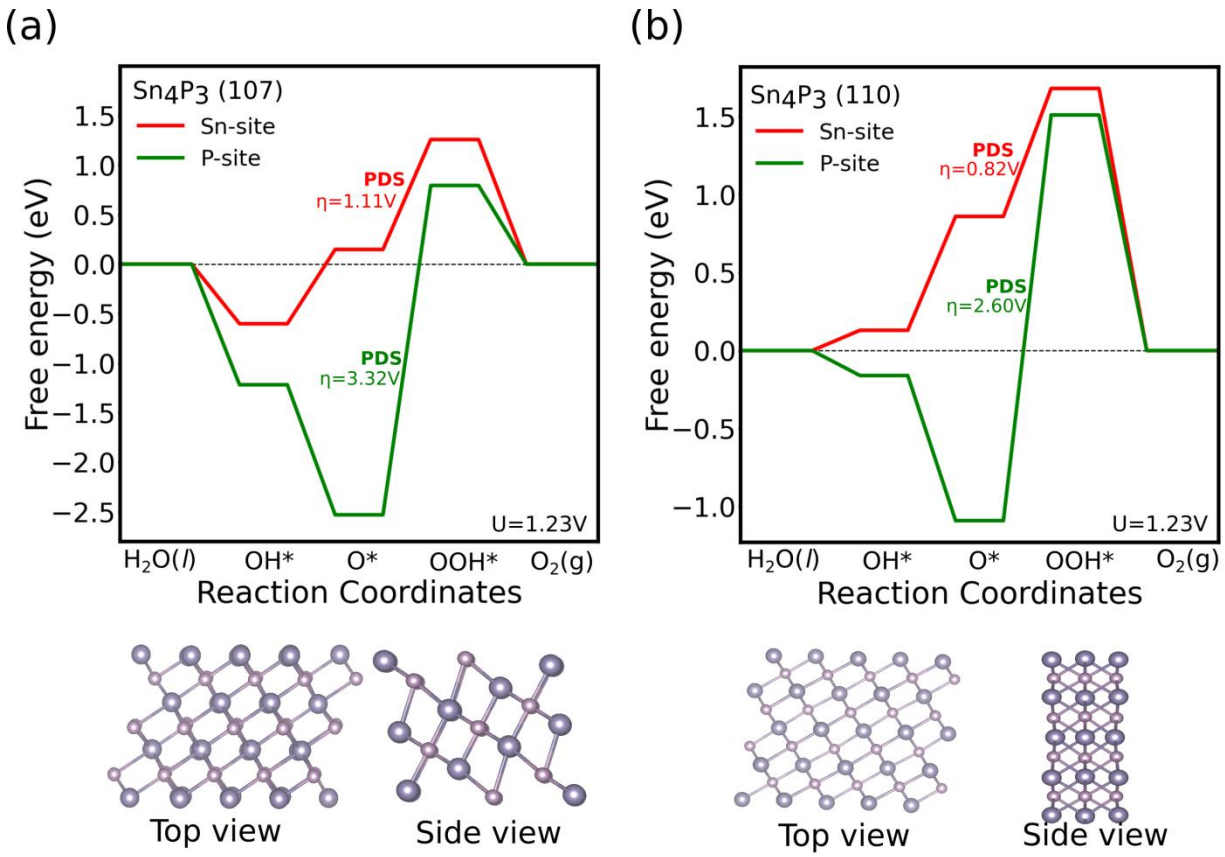

Figure S27. Gibbs free-energy diagrams of OER on the surface of (107) and (110) planes of Sn_4P_3 with their structural representations. Here, Sn_4P_3 (110) indicates more active plane towards OER process. Both P-site and Sn-site is active for OER reactions, out of which Sn-site is more active towards OER kinetics

Table S9. Total energy and adsorption energy of different adsorbates on the surface of pristine SWCNT, Sn_4P_3 and Sn_4P_3-SWCNT heterostructure.

Surface	Total Energy (eV)	Adsorption energy (eV)
SWCNT	-519.30229533	-
SWCNT + OH*	-528.72603209	2.05
SWCNT + O*	-526.23640489	1.15
SWCNT + OOH*	-	5.35*
Sn_4P_3	-78.10384016	-
Sn_4P_3@Sn + OH*	-88.22411043	1.36
Sn_4P_3@Sn + O*	-82.86262287	3.32
Sn_4P_3@Sn + OOH*	-92.29533408	5.37
Sn_4P_3@P + OH*	-88.50840294	1.07
Sn_4P_3@P + O*	-92.46477395	1.37
Sn_4P_3@P + OOH*	-690.30542476	5.20
Sn_4P_3-SWCNT@Sn + OH*	-700.57853432	1.20
Sn_4P_3-SWCNT@Sn + O*	-695.10096994	3.29
Sn_4P_3-SWCNT@Sn + OOH*	-704.63422987	5.24

* For graphene and SWCNT, $\Delta E_{OOH^*} = \Delta E_{OH^*} + 3.3$ eV.[76]

Table 10. Gibb's free energy and overpotential values of pristine SWCNT, Sn_4P_3 and Sn_4P_3-SWCNT heterostructure.

Surface	ΔG_1 (eV)	ΔG_2 (eV)	ΔG_3 (eV)	ΔG_4 (eV)	η (V)
SWCNT	0.82	-2.13	2.98	-1.67	2.98
Sn_4P_3	0.13	0.73	0.82	-1.68	0.82
Sn_4P_3-SWCNT	-0.023	0.853	0.72	-1.55	0.853

Table S11. Total energy and adsorption energy values of H* on the surface of pristine SWCNT, Sn_4P_3 and Sn_4P_3-SWCNT heterostructure.

Surface	Total Energy (eV)	Adsorption energy (eV)	Gibbs Energy (eV)
SWCNT + H*	-521.6763881	1.02	1.26
Sn_4P_3@Sn+ H*	-80.64409199	0.85	1.09
Sn_4P_3@P+ H*	-81.45881386	0.038	0.28
Sn_4P_3-SWCNT@P + H*	-693.7437643	-0.044	0.196

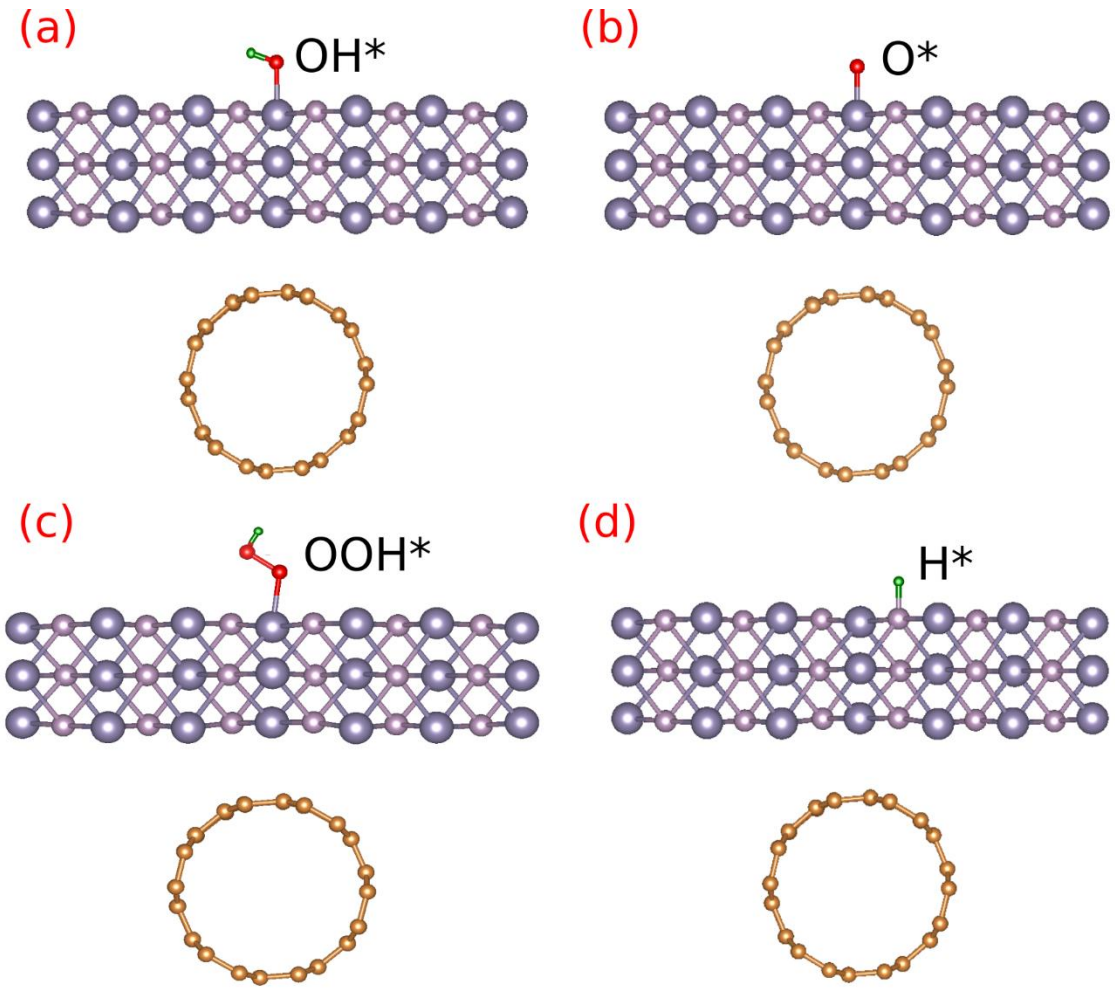

Figure S28. Structural representations of the adsorption of OER (OH*, O* and OOH*) and HER (H*) intermediates on the surface of Sn_4P_3-SWCNT heterostructure.

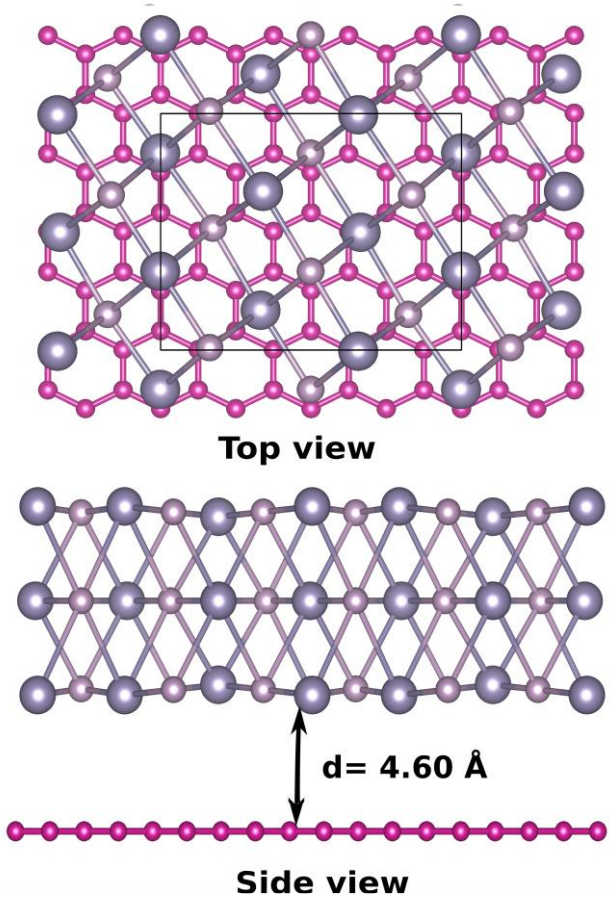

Figure S29. Schematic representation of top and side views of Sn_4P_3-Graphene heterostructure. The Sn_4P_3-Graphene heterostructure has been constructed using Sn_4P_3 (18 atoms) and graphene sheet (32 atoms). The optimized interlayer distance between Sn_4P_3 and graphene in heterostructure is found to be 4.6 Å.

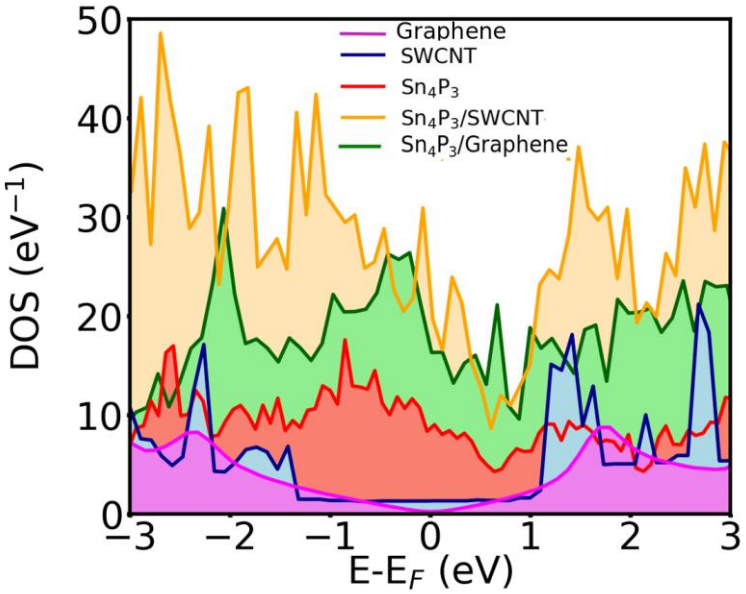

Figure S30. Density of states (DOS) plot for pristine Sn_4P_3, pristine SWCNT, pure Graphene, Sn_4P_3-SWCNT and Sn_4P_3-Graphene heterostructure.

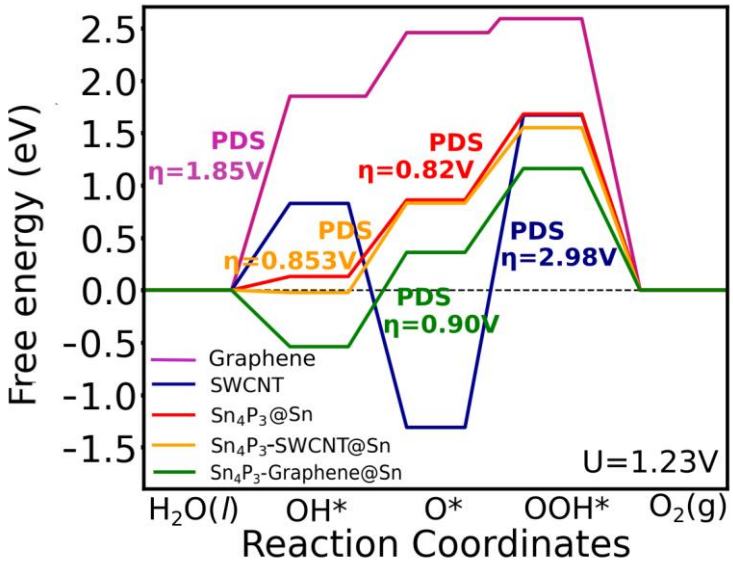

Figure S31. The calculated free energy for OER intermediates adsorbed on the surfaces of pristine SWCNT, Sn_4P_3, pure graphene, Sn_4P_3-SWCNT and Sn_4P_3-Graphene heterostructures.

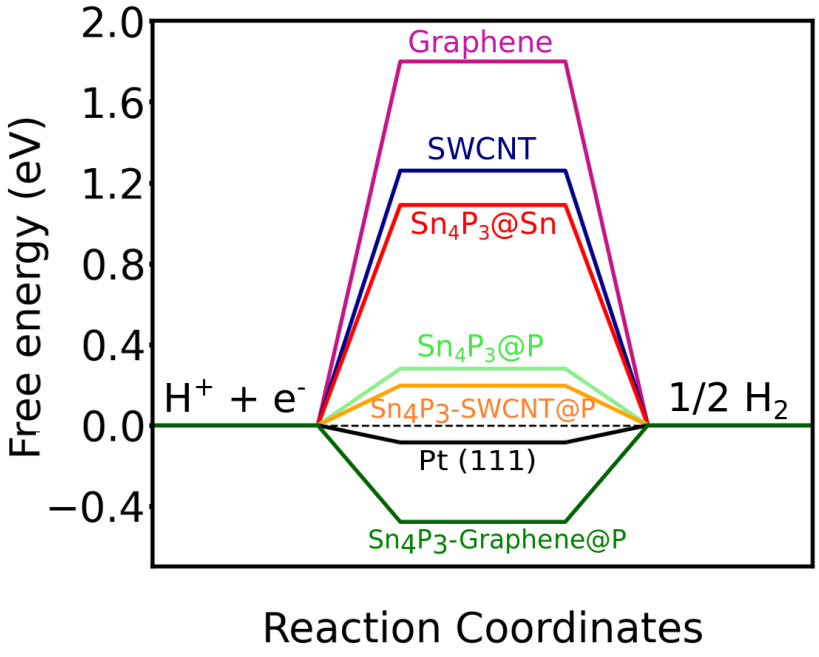

Figure S32. The calculated free energy for HER intermediate adsorbed on the surfaces of pristine SWCNT, pure graphene Sn_4P_3, Sn_4P_3-SWCNT and Sn_4P_3-Graphene heterostructures.

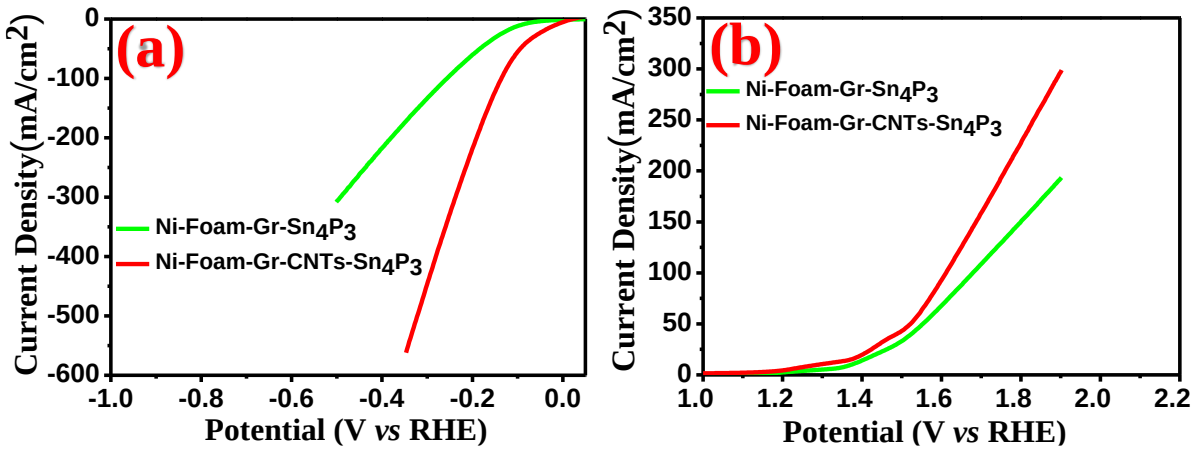

Figure S33. LSV polarization curve of Ni-Gr-Sn_4P_3 and Ni-Gr-CNTs-Sn_4P_3 samples for (a) HER and (b) OER

Overall water splitting mechanism:

The breaking of water is not a thermodynamically favourable reaction and its required 286 k/mol of energy input corresponding to a thermodynamic voltage of 1.23 V under standard conditions of room temperature and pressure. The water splitting mechanism is given as:

The total reaction: $2H_2O \rightarrow 2H_2 + O_2$

In acidic electrolyte: cathode surface: $4H^+ + 4e^- \rightarrow 2H_2$

anode surface: $2H_2O \rightarrow 4H^+ + O_2 + 4e^-$

In neutral and alkaline electrolytes:

cathode surface: $4H_2O + 4e^- \rightarrow 2H_2 + 4OH^-$

anode surface: $4OH^- \rightarrow 2H_2O + O_2 + 4e^-$

Table S12. Cell-voltage comparison of recently reported monometallic phosphide-based catalysts with the as-synthesized Ni-Gr-CNTs-Sn_4P_3 for overall water splitting in 1M KOH solution.

S.No.	Catalysts	Medium	Current Density (mA/cm^2)	Cell Voltage (V)	Ref
1	Cu_3P/NF	1 M KOH	10	1.63	[21]
2	Ni_2P/rGO/NF	1 M KOH	10	1.676	[28]
3	CoP/rGO	1 M KOH	10	1.70	[33]
4	Cuf@Ni_5P_4	1 M KOH	10	1.66	[78]
5	MOF Derived Ni_2P NS	1 M KOH	10	1.52	[38]
6	Ni_2P/Ni/NF	1 M KOH	10	1.49	[40]
7	Ni_2P@NSG	1 M KOH	10	1.572	[44]
8	Ni_2P NPs/NF	1 M KOH	10	1.63	[55]
9	Ni_5P_4/NF	1 M KOH	10	1.7	[41]
10	Ni-P@CP	1 M KOH	10	1.48	[57]
11	CoP-MNA/NF	1 M KOH	10	1.62	[58]
12	Co-P film	1 M KOH	10	1.56	[59]
13	CoP NWs	1 M KOH	10	1.56	[60]
14	Co_2P/CoNPC	1 M KOH	10	1.64	[62]
15	Co_2P NCs		10	1.56	[63]
16	Multishelled Ni_2P	1 M KOH	10	1.57	[71]
17	CoP-CNT	1 M KOH	10	1.52	[72]
18	C@Ni_8P_3	1 M KOH	10	1.65	[73]
19	CoP_2/RGO	1 M KOH	10	1.56	[74]
20	N doped FeP	1 M KOH	100	1.72	[79]
21	Ni/Ni_8P_3	1 M KOH	10	1.79	[80]
22	Mo-CoP_3/CC	1 M KOH	10	1.65	[81]
23	Fe-CoP/Ti	1 M KOH	10	1.60	[82]
24	FeP/CC	1 M KOH	10	1.69	[83]
25	**Ni-Gr-CNTs-Sn_4P_3**	**1 M KOH**	**10**	**1.482**	**This work**

Estimation of the energy efficiency of water electrolyzer:

The water electrolysis proceeds via hydrogen evolution reaction (HER) on the cathode surface and the oxygen evolution reaction (OER) on the anode end. The minimal cell voltage E_{cell}^0 required for the electrolysis of water under standard condition (25° C temperature, 1 atm pressure) is given by the following equation[60]

$$E_{cell}^0 = -\frac{\Delta G^O}{\eta F} \quad (1)$$

$$\Delta G^0 = -\eta F E_{cell}^0 \quad (2)$$

where ΔG^0 is the change in the Gibbs-free energy under standard conditions, $\eta\ is$ the number of electrons transferred and F is the Faraday constant (F ~ 96485 C/mol)

$\Delta G^0 = \Delta H^0 - TR\Delta n - T\Delta S^0$ (3)

For the electrolysis of water, the standard reaction enthalpy is ΔH^0= 285.8 kJ mol^{-1}, Δn = 1.5, ΔS^0(H_2) = 130.6 J mol^{-1}, ΔS^0(O_2) = 205.1 J mol^{-1}, ΔS^0(H_2O) = 70 J mol^{-1}K^{-1}, ΔS^0_{Tot}= 130.6 + ½205.1-70 = 163.14 J mol^{-1}K^{-1}, and ΔG^0= 237.2 kJ mol^{-1}. Thus, the minimum cell voltage for an open cell is

$E^0_{cell} = -\frac{\Delta G^O}{\eta F} = 1.23\ V$ according to equation (2).

The maximum possible efficiency of an ideal open electrochemical cell is defined by the following equation:

$\in_{max} = \frac{\Delta H^0}{\Delta G} = -\frac{\Delta H^0}{nFE_{cell}}$ (4)

where $E_{Cell}$is the cell voltage to drive water splitting at the current of I [60]

$E_{Cell} = E^0_{Cell} + IR + \sum n$ (5)

where R is the total ohmic series resistance in the cell which include the resistance of the external circuit, electrolyte, electrodes and membrane materials (if any); $\sum n$ is the sum of overpotentials including the activation overpotential at the two electrodes and the concentration overpotential.

The splitting of water by electrolysis is an endothermic reaction and the enthalpy change in this process is defined as follows[60]:

$\Delta H^0 = \Delta G^0 + T\Delta S = -\eta F E^0_{Cell} + T\Delta S$ (6)

where ΔG^0supplies energy in the form of applied electricity and the rest, $T\Delta S$, by heat.

In electrolysis, the cell voltage is always higher as compared to the theoretical voltage termed as reversible voltage E^0_{Cell}= 1.23 V, where the voltage difference is converted into heat. When the cell voltage reaches 1.48 V, the heat generated by the overpotential and ohmic loss is used by the reaction and at this voltage, there is no heat generation or absorption to and from outside the system i.e., ΔS=0. Consequently, the cell voltage of 1.48 V is defined as "thermo-neutral potential" where the cell does not heat or cool and all-electric energy used for electrolysis is converted into heat content of evolved gas.[60] This voltage is used as the standard of 100% efficiency. As the thermo-neutral potential is a signature of 100% current efficiency in water electrolysis. Thus, the energy efficiency of water electrolysis can be calculated by dividing 1.48 V with the practical cell voltage (E_{Cell}) and it can be derived by the following according equations (4) and (6):

$\in \cong \frac{1.48\ V}{E_{Cell}}$ (7)

Estimation of Faradaic efficiency:

Here, faradaic efficiency can be estimated by the gas chromatography (GC) technique *via* quantifying the gas products. It is expressed as:[84]

$$\text{Faradaic Efficiency} = \frac{z \times F \times n}{I \times t}$$

z is the number of electrons involved in the HER and OER. Here, we consider that 2 electrons are involved in HER for one mole of hydrogen production and 4 electrons are involved in OER for one mole of oxygen production. n is the total number of moles of the gas evolved during water electrolysis reaction, F is the faraday constant (F ~96485 C/mol), I is the constant applied current and in our case it is fixed at ~10 mA/cm^2 during water splitting reaction. The quantification of produced gas during water electrolysis has been carried out every 20 minutes by taking 20 μl gas from the sealed vessel using an air-tight glass syringe followed by injection into the GC system. Before starting the quantification measurement, the solution is saturated with argon and N_2 gases for 1 hour each.

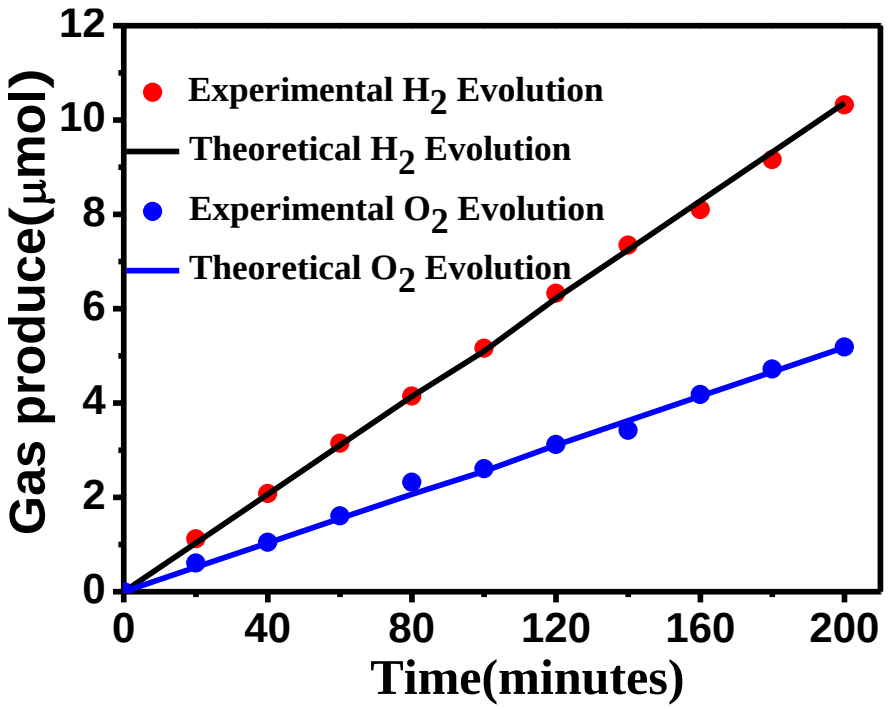

Figure S34. The experimentally and theoretically estimated amount of H_2 and O_2 produced by the Ni-Gr-CNTs-Sn_4P_3 electrode at a fixed current density of 10 mA/cm^2 in 1M KOH solution during water electrolysis. A very small deviation in experimental and theoretical result indicates ~ 99 % faradaic efficiency with the production of H_2 and O_2 at a molar ratio of 2:1.

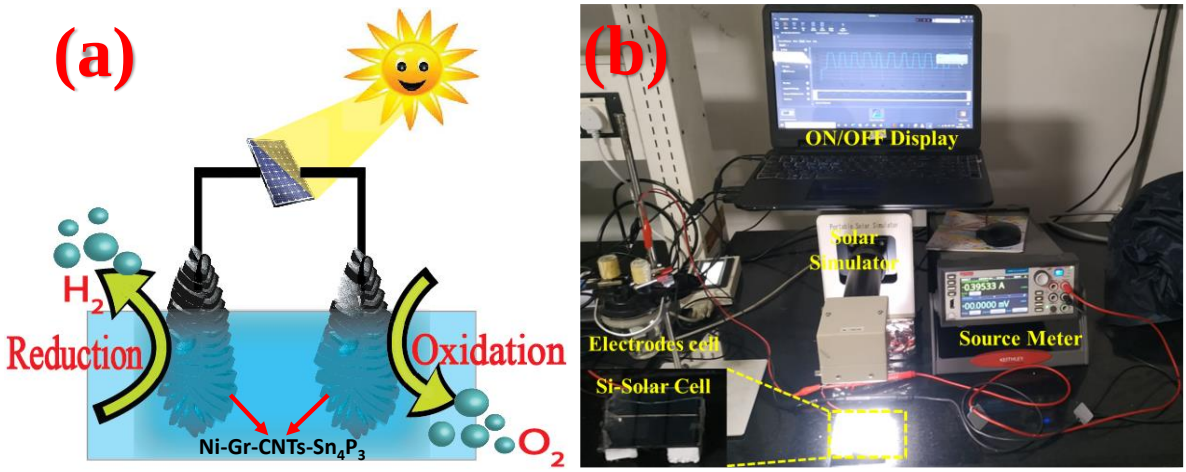

Figure S35. (a) Schematic illustration and (b) the optical photograph of the overall integrated set-up of the solar-driven water splitting.

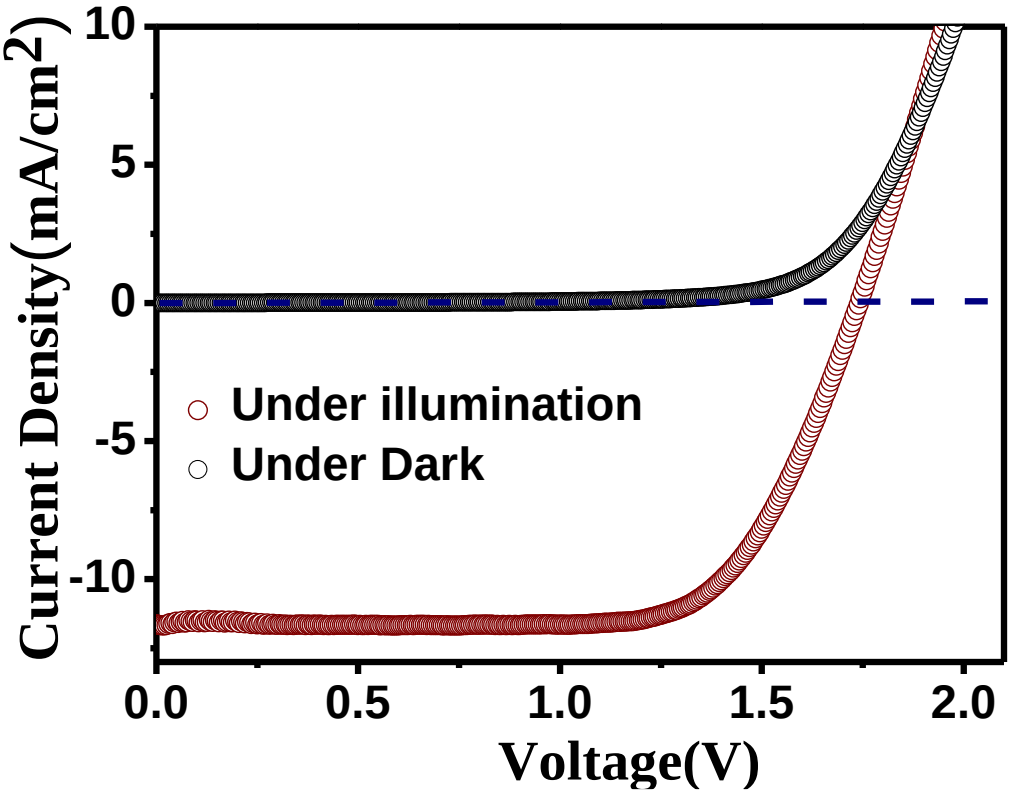

Figure S36. The *I-V* measurement of standard Si-solar cell under both dark and illumination (AM 1.5G, 100 mW/cm^2) conditions.

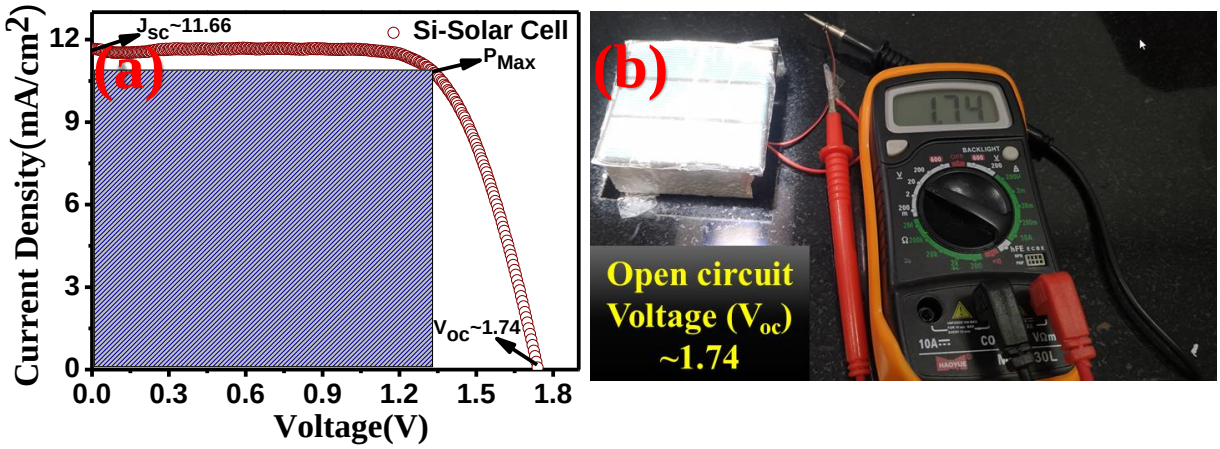

Figure S37. The *I-V* measurement of standard Si-solar cell in illumination (AM 1.5G, 100 mW/cm^2) condition demonstrates a short-circuit photocurrent density (I_{sc}), open-circuit voltage (V_{oc}) and fill factor (FF) of 11.66 mA/cm^2, 1.74 V and 0.71, respectively with power conversion efficiency (PCE) of ~14.43% and (b) open-circuit voltage (V_{oc}) of Si-solar cell verified by multi-meter.

Table S13. Operating point and STH efficiency Ni-Gr-CNTs-Sn_4P_3 have been compared with the recently reported solar-driven electrocatalyst for overall water splitting.

S.No.	Solar cell category	Solar cell structure	Catalysts	Operating Point (mA/cm^2)	STH %	Ref
1	DSSC	FTO/TiO_2/Dye/PEDOT/FTO	WO_3	2.52	3.10	85
2	DSSC	FTO/TiO_2/Dye/PEDOT/FTO	Fe_2O_3	0.95	1.17	85
3	DSSC	FTO/TiO_2/Dye/Pt/FTO	WO_3/$BiVO_4$	4.6	5.7	86
4	PSC	FTO/TiO_2/$MAPbI_3$/Spiro/Au	NiFe-LDH	10	12.3	87
5	PSC	FTO/TiO_2/$MAPbI_3$/Spiro/Au	BiVO4	2	2.5	88
6	PSC	FTO/TiO_2/$MAPbI_3$/Spiro/Au	FeNiOx/Al_2O_3/Fe_2O_3	1.6	2.0	89
7	PSC	FTO/TiO_2/$MAPbI_3$/Spiro/Au	Mn-Fe_2O_3	1.93	2.4	90
8	PSC	ITO/PEDOT/$MAPbI_3$/PCBM/Al	$NiCo_2O_4$	5	6.2	91
9	PSC	FTO/NiMgLiO/$MAPbI_3$/PCBM/Ti(Nb)O_x/Ag	$BiVO_4$	5.01	6.2	92
10	PSC	FTO/TiO_2/$MAPbI_3$/Carbon	CoP	5.5	6.7	93
11	PolSC	Triple Junction polymer	Pt	-	3.1	94
12	PSC	FTO/TiO_2/$CH_3NH_3PbI_{3-x}Cl_x$ Spiro/MoO_3/Au	NiFe alloy NP supported N, S-doped carbon	7.6	9.7	95
13	PSC	Based on $CsPb_{0.9}Sn_{0.1}IBr_2$	$Ni_{0.5}Co_{0.5}P$ /CP	-	3.12	96
14	PSC	ITO/PEDOT: PSS/	Te/SnS_2/A	-	0.49	97

		$CH_3NH_3PbI_{3-x}Cl_x$ /PCBM/CBLs/Al	g			
15	Silicon	2-jn a-Si	W:$BiVO_4$	4	4.9	[92]
16	Silicon	3-jn a-Si	Co-OEC/NiMo Zn	-	2.5	[98]
17	Silicon	2-jn planar -Si	NiFeSP/NF	-	9.2	[99]
18	**Silicon**	**2-jn planar -Si**	**Ni-Gr-CNTs-Sn_4P_3**	**8.89**	**10.82**	**This work**

PSC- perovskite solar cells, PolSC- polymer solar cell, DSSC, Dye-Sensitized Solar Cells

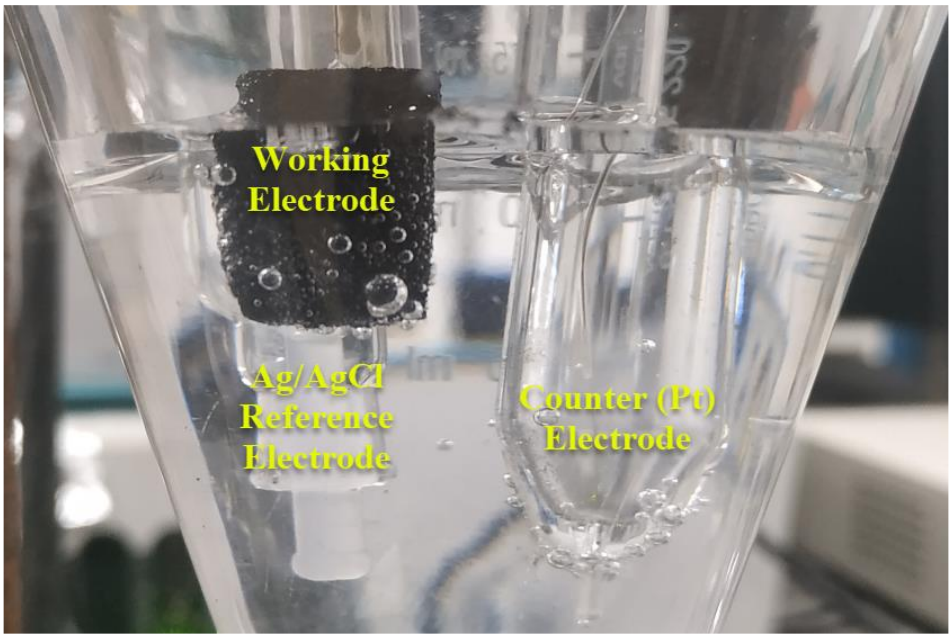

Figure S38. Optical photograph of the three-electrode setup for electrochemical measurement. Here, Pt wire acts as a counter electrode, Ni-Gr-CNTs-Sn_4P_3 is a working electrode and Ag/AgCl. The bubble formation on the working electrode surface confirms gas generation *via* water splitting.

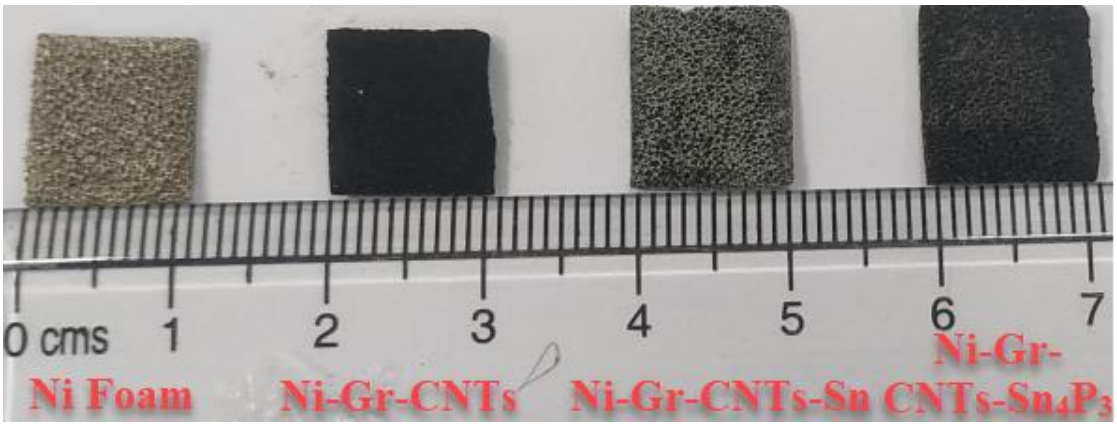

Figure S39. The optical photograph of the as-prepared electrodes where the effective working electrode area is ~ (1x1.2) cm^2 which is immerged in the electrolyte during the electrochemical measurement.

Supplementary videos:

Video S1: Under the chronoamperometric measurement, the continuous H_2 and O_2 bubbles are generated from the two similar electrodes of Ni-Gr-CNTs-Sn_4P_3 acting as cathode and anode, respectively. The video demonstrates that small-sized gas bubbles are continuously releasing from the electrode surface and its immediate disappearance confirms the super-aerophobic nature of the as-designed catalyst. This property helps to minimize the dead surface area and creates a better exposure of the active sites towards the electrolyte thereby enhancing the overall water splitting performance.

Video S2: The live video demonstrates the solar-driven overall water splitting which has been tested by integrating with a commercially available Si solar cell (open circuit voltage ~ 1.74 V). Here the water electrolyser is powered by the solar-cell for the continuous generation of H_2 and O_2 from the cathode and anode surface, respectively. This demonstrate a footprint towards the development of green fuel production *via* renewable energy resources which is a better alternative as compared to the existing photoelectrochemical technology.

Video S3: The live video demonstrates the super-hydrophilic nature of the catalyst as it is clearly observed that all the water droplets are getting absorbed and immediately seeps through the surface of Ni-Gr-CNTs-Sn_4P_3. The super-hydrophilic property of the catalyst creates more wettable surface as well as activates the electrocatalyst surface towards electrolyte and thereby improves the overall water splitting performance.

References:

(1) Dutta, S.; Indra, A.; Feng, Y.; Song, T.; Paik, U. Self-Supported Nickel Iron Layered Double Hydroxide-Nickel Selenide Electrocatalyst for Superior Water Splitting Activity. *ACS Appl. Mater. Interfaces* **2017**, *9*, 33766-33774.

(2) Hengne, A. M.; Samal, A. K.; Enakonda, L. R.; Harb, M.; Gevers, L. E.; Anjum, D. H.; Hedhili, M. N.; Saih, Y.; Huang, K.-W.; Basset, J.-M. Ni–Sn-Supported ZrO_2 Catalysts Modified by Indium for Selective CO_2 Hydrogenation to Methanol. *ACS Omega* **2018**, *3*, 3688-3701.

(3) Riyajuddin, S.; Azmi, K.; Pahuja, M.; Kumar, S.; Maruyama, T.; Bera, C.; Ghosh, K. Super-Hydrophilic Hierarchical Ni-Foam-Graphene-Carbon Nanotubes-Ni_2P-CuP_2 Nano-Architecture As Efficient Electrocatalyst for Overall Water Splitting. *ACS Nano* **2021**, *15*, 5586-5599.

(4) Riyajuddin, S.; Aziz, S. K. T.; Kumar, S.; Nessim, G. D.; Ghosh, K. 3D-Graphene Decorated with g-C_3N_4/Cu_3P Composite: A Noble Metal-Free Bifunctional Electrocatalyst for Overall Water Splitting. *ChemCatChem* **2020**, *12*, 1394-1402.

(5) Zhao, W.; Ma, X.; Gao, L.; Li, Y.; Wang, G.; Sun, Q. Engineering Carbon-Nanochain Concatenated Hollow Sn_4P_3 Nanospheres Architectures As Ultrastable and High-Rate Anode Materials for Sodium Ion Batteries. *Carbon* **2020**, *167*, 736-745.

(6) Pan, E.; Jin, Y.; Zhao, C.; Jia, M.; Chang, Q.; Jia, M.; Wang, L.; He, X. Conformal Hollow Carbon Sphere Coated on Sn_4P_3 Microspheres As High-Rate and Cycle-Stable Anode Materials with Superior Sodium Storage Capability. *ACS Appl. Energy Mater.* **2019**, *2*, 1756-1764.

(7) Liu, S.; Zhang, H.; Xu, L.; Ma, L.; Hou, X. High Lithium Storage Performance of Mn-Doped Sn_4P_3 Nanoparticles. *Electrochimica Acta* **2016**, *210*, 888-896.

(8) Liu, W.; Yuan, X.; Yu, X. One-Step Solvothermal Route to Sn_4P_3-Reduced Graphene Oxide Nanohybrids As Cycle-Stable Anode Materials for Sodium-Ion Batteries. *ACS Appl. Mater. Interfaces* **2021**, *13*, 12016-12024.

(9) Wang, M.; Weng, G.-M.; Yasin, G.; Kumar, M.; Zhao, W. A High-Performance Tin Phosphide/Carbon Composite Anode for Lithium-Ion Batteries. *Dalton Trans.* **2020**, *49*, 17026-17032.

(10) Sun, S.; Li, R.; Wang, W.; Mu, D.; Liu, J.; Chen, T.; Tian, S.; Zhu, W.; Dai, C. One-Dimensional Coaxial Cable-like MWCNTs/Sn_4P_3@C As an Anode Material with Long-Term Durability for Lithium Ion Batteries. *Inorg. Chem. Front.* **2020**, *7*, 2651-2659.

(11) Li, D.; Zhang, Y.; Sun, Q.; Zhang, S.; Wang, Z.; Liang, Z.; Si, P.; Ci, L. Hierarchically Porous Carbon Supported Sn_4P_3 As a Superior Anode Material for Potassium-Ion Batteries. *Energy Storage Materials* **2019**, *23*, 367-374.

(12) Du, J.; Chen, Z.; Ye, S.; Wiley, B. J.; Meyer, T. J. Copper As a Robust and Transparent Electrocatalyst for Water Oxidation. *Angewandte Chemie International Edition* **2015**, *54*, 2073-2078.

(13) Kanan, M. W.; Surendranath, Y.; Nocera, D. G. Cobalt–Phosphate Oxygen-Evolving Compound. *Chem. Soc. Rev.* **2008**, *38*, 109-114.

(14) Yu, S. H.; Chua, D. H. C. Toward High-Performance and Low-Cost Hydrogen Evolution Reaction Electrocatalysts: Nanostructuring Cobalt Phosphide (CoP) Particles on Carbon Fiber Paper. *ACS Appl. Mater. Interfaces* **2018**, *10*, 14777-14785.

(15) Ye, C.; Wang, M. Q.; Chen, G.; Deng, Y. H.; Li, L. J.; Luo, H. Q.; Li, N. B. One-Step CVD Synthesis of Carbon Framework Wrapped Co_2P As a Flexible Electrocatalyst for Efficient Hydrogen Evolution. *J. Mater. Chem. A* **2017**, *5*, 7791-7795.

(16) Lin, Y.; He, L.; Chen, T.; Zhou, D.; Wu, L.; Hou, X.; Zheng, C. Cost-Effective and Environmentally Friendly Synthesis of 3D Ni_2P from Scrap Nickel for Highly Efficient Hydrogen Evolution in Both Acidic and Alkaline Media. *J. Mater. Chem. A* **2018**, *6*, 4088-4094.

(17) Li, D.; Liao, Q.; Ren, B.; Jin, Q.; Cui, H.; Wang, C. A 3D-Composite Structure of FeP Nanorods Supported by Vertically Aligned Graphene for the High-Performance Hydrogen Evolution Reaction. *J. Mater. Chem. A* **2017**, *5*, 11301-11308.

(18) Tian, J.; Liu, Q.; Asiri, A. M.; Sun, X. Self-Supported Nanoporous Cobalt Phosphide Nanowire Arrays: An Efficient 3D Hydrogen-Evolving Cathode over the Wide Range of PH 0-14. *J Am Chem Soc* **2014**, *136*, 7587-7590.
(19) Tian, J.; Liu, Q.; Cheng, N.; Asiri, A. M.; Sun, X. Self-Supported Cu_3P Nanowire Arrays As an Integrated High-Performance Three-Dimensional Cathode for Generating Hydrogen from Water. *Angewandte Chemie International Edition* **2014**, *53*, 9577-9581.
(20) Pi, M.; Wang, X.; Zhang, D.; Wang, S.; Chen, S. A 3D Porous WP_2 Nanosheets@carbon Cloth Flexible Electrode for Efficient Electrocatalytic Hydrogen Evolution. *Front. Chem. Sci. Eng.* **2018**, *12*, 425-432.
(21) Yang, Z.; Tuo, Y.; Lu, Q.; Chen, C.; Liu, M.; Liu, B.; Duan, X.; Zhou, Y.; Zhang, J. Hierarchical Cu_3P-Based Nanoarrays on Nickel Foam As Efficient Electrocatalysts for Overall Water Splitting. *Green Energy & Environment* **2020**.
(22) Liang, Y.; Liu, Q.; Asiri, A. M.; Sun, X.; Luo, Y. Self-Supported FeP Nanorod Arrays: A Cost-Effective 3D Hydrogen Evolution Cathode with High Catalytic Activity. *ACS Catal.* **2014**, *4*, 4065-4069.
(23) Cai, Z.; Song, X.; Wang, Y.; Chen, X. Electrodeposition-Assisted Synthesis of Ni_2P Nanosheets on 3D Graphene/Ni Foam Electrode and Its Performance for Electrocatalytic Hydrogen Production. *ChemElectroChem* **2015**, *2*, 1665-1671.
(24) Pu, Z.; Liu, Q.; Jiang, P.; Asiri, A. M.; Obaid, A. Y.; Sun, X. CoP Nanosheet Arrays Supported on a Ti Plate: An Efficient Cathode for Electrochemical Hydrogen Evolution. *Chem. Mater.* **2014**, *26*, 4326-4329.
(25) Pu, Z.; Amiinu, I. S.; Wang, M.; Yang, Y.; Mu, S. Semimetallic MoP_2: An Active and Stable Hydrogen Evolution Electrocatalyst over the Whole PH Range. *Nanoscale* **2016**, *8*, 8500–8504.
(26) Han, A.; Jin, S.; Chen, H.; Ji, H.; Sun, Z.; Du, P. A Robust Hydrogen Evolution Catalyst Based on Crystalline Nickel Phosphide Nanoflakes on Three-Dimensional Graphene/Nickel Foam: High Performance for Electrocatalytic Hydrogen Production from PH 0-14. *J. Mater. Chem. A* **2015**, *3*, 1941-1946.
(27) Wu, T.; Pi, M.; Zhang, D.; Chen, S. 3D Structured Porous CoP_3 Nanoneedle Arrays As an Efficient Bifunctional Electrocatalyst for the Evolution Reaction of Hydrogen and Oxygen. *J. Mater. Chem. A* **2016**, *4*, 14539-14544.
(28) Huang, J.; Li, F.; Liu, B.; Zhang, P. Ni_2P/RGO/NF Nanosheets As a Bifunctional High-Performance Electrocatalyst for Water Splitting. *Materials (Basel)* **2020**, *13*, E744.
(29) Huang, Z.; Chen, Z.; Chen, Z.; Lv, C.; Meng, H.; Zhang, C. $Ni_{12}P_5$ Nanoparticles As an Efficient Catalyst for Hydrogen Generation via Electrolysis and Photoelectrolysis. *ACS Nano* **2014**, *8*, 8121-8129.
(30) Popczun, E. J.; McKone, J. R.; Read, C. G.; Biacchi, A. J.; Wiltrout, A. M.; Lewis, N. S.; Schaak, R. E. Nanostructured Nickel Phosphide As an Electrocatalyst for the Hydrogen Evolution Reaction. *J. Am. Chem. Soc.* **2013**, *135*, 9267-9270.
(31) Popczun, E. J.; Read, C. G.; Roske, C. W.; Lewis, N. S.; Schaak, R. E. Highly Active Electrocatalysis of the Hydrogen Evolution Reaction by Cobalt Phosphide Nanoparticles. *Angewandte Chemie International Edition* **2014**, *53*, 5427-5430.
(32) Zhu, W.; Tang, C.; Liu, D.; Wang, J.; Asiri, A. M.; Sun, X. A Self-Standing Nanoporous MoP_2 Nanosheet Array: An Advanced PH-Universal Catalytic Electrode for the Hydrogen Evolution Reaction. *J. Mater. Chem. A* **2016**, *4*, 7169-7173.
(33) Jiao, L.; Zhou, Y.-X.; Jiang, H.-L. Metal–Organic Framework-Based CoP/Reduced Graphene Oxide: High-Performance Bifunctional Electrocatalyst for Overall Water Splitting. *Chem. Sci.* **2016**, *7*, 1690-1695.
(34) Liu, Q.; Tian, J.; Cui, W.; Jiang, P.; Cheng, N.; Asiri, A. M.; Sun, X. Carbon Nanotubes Decorated with CoP Nanocrystals: A Highly Active Non-Noble-Metal Nanohybrid Electrocatalyst for Hydrogen Evolution. *Angewandte Chemie* **2014**, *126*, 6828-6832.

(35) Xiao, P.; Sk, M. A.; Thia, L.; Ge, X.; Lim, R. J.; Wang, J.-Y.; Lim, K. H.; Wang, X. Molybdenum Phosphide As an Efficient Electrocatalyst for the Hydrogen Evolution Reaction. *Energy Environ. Sci.* **2014**, *7*, 2624-2629.
(36) Das, M.; Jena, N.; Purkait, T.; Kamboj, N.; Sarkar, A. D.; Dey, R. S. Single-Phase Ni_5P_4-Copper Foam Superhydrophilic and Aerophobic Core–Shell Nanostructures for Efficient Hydrogen Evolution Reaction. *J. Mater. Chem. A* **2019**, *7*, 23989-23999.
(37) Kim, J.-Y.; Park, H.; Joo, W.; Nam, D.-H.; Lee, S.; Kim, H. G.; Ahn, I.-K.; Kang, H.-Y.; Lee, G.-B.; Jung, I.; Kim, M.-Y.; Lee, G.-D.; Joo, Y.-C. Predictive Fabrication of Ni Phosphide Embedded in Carbon Nanofibers As Active and Stable Electrocatalysts. *J. Mater. Chem. A* **2019**, *7*, 7451-7458.
(38) Wang, Q.; Liu, Z.; Zhao, H.; Huang, H.; Jiao, H.; Du, Y. MOF-Derived Porous Ni_2P Nanosheets As Novel Bifunctional Electrocatalysts for the Hydrogen and Oxygen Evolution Reactions. *J. Mater. Chem. A* **2018**, *6*, 18720-18727.
(39) Yan, L.; Dai, P.; Wang, Y.; Gu, X.; Li, L.; Cao, L.; Zhao, X. In Situ Synthesis Strategy for Hierarchically Porous Ni_2P Polyhedrons from MOFs Templates with Enhanced Electrochemical Properties for Hydrogen Evolution. *ACS Appl. Mater. Interfaces* **2017**, *9*, 11642-11650.
(40) You, B.; Jiang, N.; Sheng, M.; Bhushan, M. W.; Sun, Y. Hierarchically Porous Urchin-Like Ni_2P Superstructures Supported on Nickel Foam As Efficient Bifunctional Electrocatalysts for Overall Water Splitting. *ACS Catal.* **2016**, *6*, 714-721.
(41) Ledendecker, M.; Krick Calderón, S.; Papp, C.; Steinrück, H.-P.; Antonietti, M.; Shalom, M. The Synthesis of Nanostructured Ni_5P_4 Films and Their Use As a Non-Noble Bifunctional Electrocatalyst for Full Water Splitting. *Angewandte Chemie International Edition* **2015**, *54*, 12361-12365.
(42) Jiang, P.; Liu, Q.; Liang, Y.; Tian, J.; Asiri, A. M.; Sun, X. A Cost-Effective 3D Hydrogen Evolution Cathode with High Catalytic Activity: FeP Nanowire Array as the Active Phase. *Angew Chem Int Ed Engl* **2014**, *53*, 12855-12859.
(43) Vigil, J. A.; Lambert, T. N. Nanostructured Cobalt Phosphide-Based Films As Bifunctional Electrocatalysts for Overall Water Splitting. *RSC Adv.* **2015**, *5*, 105814-105819.
(44) Suryawanshi, U. P.; Ghorpade, U. V.; Lee, D. M.; He, M.; Shin, S. W.; Kumar, P. V.; Jang, J. S.; Jung, H. R.; Suryawanshi, M. P.; Kim, J. H. Colloidal Ni_2P Nanocrystals Encapsulated in Heteroatom-Doped Graphene Nanosheets: A Synergy of 0D@2D Heterostructure Toward Overall Water Splitting. *Chem. Mater.* **2021**, *33*, 234-245.
(45) Li, Y.; Dong, Z.; Jiao, L. Multifunctional Transition Metal-Based Phosphides in Energy-Related Electrocatalysis. *Advanced Energy Materials* **2020**, *10*, 1902104.
(46) Wei, L.; Goh, K.; Birer, Ö.; Karahan, H. E.; Chang, J.; Zhai, S.; Chen, X.; Chen, Y. A Hierarchically Porous Nickel-Copper Phosphide Nano-Foam for Efficient Electrochemical Splitting of Water. *Nanoscale* **2017**, *9*, 4401-4408.
(47) McCrory, C. C. L.; Jung, S.; Peters, J. C.; Jaramillo, T. F. Benchmarking Heterogeneous Electrocatalysts for the Oxygen Evolution Reaction. *J. Am. Chem. Soc.* **2013**, *135*, 16977-16987.
(48) Benck, J. D.; Chen, Z.; Kuritzky, L. Y.; Forman, A. J.; Jaramillo, T. F. Amorphous Molybdenum Sulfide Catalysts for Electrochemical Hydrogen Production: Insights into the Origin of Their Catalytic Activity. *ACS Catal.* **2012**, *2*, 1916-1923.
(49) Liu, S.; Liu, Q.; Lv, Y.; Chen, B.; Zhou, Q.; Wang, L.; Zheng, Q.; Che, C.; Chen, C. Ru Decorated with NiCoP: An Efficient and Durable Hydrogen Evolution Reaction Electrocatalyst in Both Acidic and Alkaline Conditions. *Chem. Commun.* **2017**, *53*, 13153-13156.
(50) Zhang, G.; Wang, B.; Bi, J.; Fang, D.; Yang, S. Constructing Ultrathin CoP Nanomeshes by Er-Doping for Highly Efficient Bifunctional Electrocatalysts for Overall Water Splitting. *J. Mater. Chem. A* **2019**, *7*, 5769-5778.
(51) Dutta, A.; Samantara, A. K.; Dutta, S. K.; Jena, B. K.; Pradhan, N. Surface-Oxidized Dicobalt Phosphide Nanoneedles As a Nonprecious, Durable, and Efficient OER Catalyst. *ACS Energy Lett.* **2016**, *1*, 169-174.

(52) Chang, J.; Xiao, Y.; Xiao, M.; Ge, J.; Liu, C.; Xing, W. Surface Oxidized Cobalt-Phosphide Nanorods As an Advanced Oxygen Evolution Catalyst in Alkaline Solution. *ACS Catal.* **2015**, *5*, 6874-6878.
(53) Ryu, J.; Jung, N.; Jang, J. H.; Kim, H.-J.; Yoo, S. J. In Situ Transformation of Hydrogen-Evolving CoP Nanoparticles: Toward Efficient Oxygen Evolution Catalysts Bearing Dispersed Morphologies with Co-Oxo/Hydroxo Molecular Units. *ACS Catal.* **2015**, *5*, 4066-4074.
(54) Han, A.; Chen, H.; Sun, Z.; Xu, J.; Du, P. High Catalytic Activity for Water Oxidation Based on Nanostructured Nickel Phosphide Precursors. *Chem. Commun.* **2015**, *51*, 11626-11629.
(55) Stern, L.-A.; Feng, L.; Song, F.; Hu, X. Ni_2P As a Janus Catalyst for Water Splitting: The Oxygen Evolution Activity of Ni_2P Nanoparticles. *Energy Environ. Sci.* **2015**, *8*, 2347-2351.
(56) Oh, S.; Kim, H.; Kwon, Y.; Kim, M.; Cho, E.; Kwon, H. Porous Co-P Foam As an Efficient Bifunctional Electrocatalyst for Hydrogen and Oxygen Evolution Reactions. *J. Mater. Chem. A* **2016**, *4*, 18272-18277.
(57) Wang, X.; Li, W.; Xiong, D.; Petrovykh, D. Y.; Liu, L. Bifunctional Nickel Phosphide Nanocatalysts Supported on Carbon Fiber Paper for Highly Efficient and Stable Overall Water Splitting. *Advanced Functional Materials* **2016**, *26*, 4067-4077.
(58) Zhu, Y.-P.; Liu, Y.-P.; Ren, T.-Z.; Yuan, Z.-Y. Self-Supported Cobalt Phosphide Mesoporous Nanorod Arrays: A Flexible and Bifunctional Electrode for Highly Active Electrocatalytic Water Reduction and Oxidation. *Advanced Functional Materials* **2015**, *25*, 7337-7347.
(59) Jiang, N.; You, B.; Sheng, M.; Sun, Y. Electrodeposited Cobalt-Phosphorous-Derived Films As Competent Bifunctional Catalysts for Overall Water Splitting. *Angewandte Chemie International Edition* **2015**, *54*, 6251-6254.
(60) Li, W.; Gao, X.; Xiong, D.; Xia, F.; Liu, J.; Song, W.-G.; Xu, J.; Thalluri, S. M.; Cerqueira, M. F.; Fu, X.; Liu, L. Vapor-Solid Synthesis of Monolithic Single-Crystalline CoP Nanowire Electrodes for Efficient and Robust Water Electrolysis. *Chem. Sci.* **2017**, *8*, 2952-2958.
(61) You, B.; Jiang, N.; Sheng, M.; Gul, S.; Yano, J.; Sun, Y. High-Performance Overall Water Splitting Electrocatalysts Derived from Cobalt-Based Metal-Organic Frameworks. *Chem. Mater.* **2015**, *27*, 7636-7642.
(62) Liu, H.; Guan, J.; Yang, S.; Yu, Y.; Shao, R.; Zhang, Z.; Dou, M.; Wang, F.; Xu, Q. Metal-Organic-Framework-Derived Co_2P Nanoparticle/Multi-Doped Porous Carbon As a Trifunctional Electrocatalyst. *Advanced Materials* **2020**, *32*, 2003649.
(63) Li, H.; Li, Q.; Wen, P.; Williams, T. B.; Adhikari, S.; Dun, C.; Lu, C.; Itanze, D.; Jiang, L.; Carroll, D. L.; Donati, G. L.; Lundin, P. M.; Qiu, Y.; Geyer, S. M. Colloidal Cobalt Phosphide Nanocrystals as Trifunctional Electrocatalysts for Overall Water Splitting Powered by a Zinc-Air Battery. *Advanced Materials* **2018**, *30*, 1705796.
(64) Menezes, P. W.; Indra, A.; Das, C.; Walter, C.; Göbel, C.; Gutkin, V.; Schmeiβer, D.; Driess, M. Uncovering the Nature of Active Species of Nickel Phosphide Catalysts in High-Performance Electrochemical Overall Water Splitting. *ACS Catal.* **2017**, *7*, 103-109.
(65) Pu, Z.; Xue, Y.; Li, W.; Amiinu, I. S.; Mu, S. Efficient Water Splitting Catalyzed by Flexible NiP_2 Nanosheet Array Electrodes under Both Neutral and Alkaline Solutions. *New J. Chem.* **2017**, *41*, 2154-2159.
(66) Aziz, S. T.; Malik, B.; Sadhanala, H. K.; Gedanken, A.; Noked, M.; Nessim, G. D. Nickel-Rich Phosphide ($Ni_{12}P_5$) Nanosheets Coupled with Oxidized Multiwalled Carbon Nanotubes for Oxygen Evolution. *ACS Appl. Nano Mater.* **2020**, *3*, 10914-10921.
(67) Xu, Y.; Duan, S.; Li, H.; Yang, M.; Wang, S.; Wang, X.; Wang, R. Au/$Ni_{12}P_5$ Core/Shell Single-Crystal Nanoparticles As Oxygen Evolution Reaction Catalyst. *Nano Res.* **2017**, *10*, 3103-3112.
(68) Lei, H.; Chen, M.; Liang, Z.; Liu, C.; Zhang, W.; Cao, R. Ni_2P Hollow Microspheres for Electrocatalytic Oxygen Evolution and Reduction Reactions. *Catal. Sci. Technol.* **2018**, *8*, 2289-2293.
(69) Masud, J.; Umapathi, S.; Ashokaan, N.; Nath, M. Iron Phosphide Nanoparticles As an Efficient Electrocatalyst for the OER in Alkaline Solution. *J. Mater. Chem. A* **2016**, *4*, 9750-9754.

(70) Wang, M.; Lin, M.; Li, J.; Huang, L.; Zhuang, Z.; Lin, C.; Zhou, L.; Mai, L. Metal–Organic Framework Derived Carbon-Confined Ni_2P Nanocrystals Supported on Graphene for an Efficient Oxygen Evolution Reaction. *Chem. Commun.* **2017**, *53*, 8372-8375.
(71) Sun, H.; Xu, X.; Yan, Z.; Chen, X.; Cheng, F.; Weiss, P. S.; Chen, J. Porous Multishelled Ni_2P Hollow Microspheres As an Active Electrocatalyst for Hydrogen and Oxygen Evolution. *Chem. Mater.* **2017**, *29*, 8539-8547.
(72) Hou, C.-C.; Cao, S.; Fu, W.-F.; Chen, Y. Ultrafine CoP Nanoparticles Supported on Carbon Nanotubes as Highly Active Electrocatalyst for Both Oxygen and Hydrogen Evolution in Basic Media. *ACS Appl. Mater. Interfaces* **2015**, *7*, 28412-28419.
(73) Yu, J.; Li, Q.; Chen, N.; Xu, C.-Y.; Zhen, L.; Wu, J.; Dravid, V. P. Carbon-Coated Nickel Phosphide Nanosheets As Efficient Dual-Electrocatalyst for Overall Water Splitting. *ACS Appl. Mater. Interfaces* **2016**, *8*, 27850-27858.
(74) Wang, J.; Yang, W.; Liu, J. CoP_2 Nanoparticles on Reduced Graphene Oxide Sheets As a Super-Efficient Bifunctional Electrocatalyst for Full Water Splitting. *J. Mater. Chem. A* **2016**, *4*, 4686-4690.
(75) Xue, Z.; Zhang, X.; Qin, J.; Liu, R. Constructing MoS_2/g-C_3N_4 Heterojunction with Enhanced Oxygen Evolution Reaction Activity: A Theoretical Insight. *Applied Surface Science* **2020**, *510*, 145489.
(76) Murdachaew, G.; Laasonen, K. Oxygen Evolution Reaction on Nitrogen-Doped Defective Carbon Nanotubes and Graphene. *J. Phys. Chem. C* **2018**, *122*, 25882-25892.
(77) Forti, M.; Alonso, P.; Gargano, P.; Rubiolo, G. Adhesion Energy of the Fe(BCC)/Magnetite Interface within the DFT Approach. *Procedia Materials Science* **2015**, *8*, 1066-1072.
(78) Das, M.; Kamboj, N.; Purkait, T.; Sarkar, S.; Dey, R. S. Revealing the Structural Aspect of Ultrastable Self-Supportive Bifunctional Electrocatalyst for Solar-Driven Water Splitting. *J. Phys. Chem. C* **2020**, *124*, 13525-13534.
(79) Yang, M.; Xie, J.-Y.; Lin, Z.-Y.; Dong, B.; Chen, Y.; Ma, X.; Wen, M.-L.; Zhou, Y.-N.; Wang, L.; Chai, Y.-M. N-Doped FeP Nanorods Derived from Fe-MOFs As Bifunctional Electrocatalysts for Overall Water Splitting. *Applied Surface Science* **2020**, *507*, 145096.
(80) Chen, G.-F.; Ma, T. Y.; Liu, Z.-Q.; Li, N.; Su, Y.-Z.; Davey, K.; Qiao, S.-Z. Efficient and Stable Bifunctional Electrocatalysts Ni/Ni_xM_y (M = P, S) for Overall Water Splitting. *Advanced Functional Materials* **2016**, *26*, 3314-3323.
(81) Zhang, S.; Guo, M.; Song, S.; Zhan, K.; Yan, Y.; Yang, J.; Zhao, B. Hierarchical Mo-Doped CoP_3 Interconnected Nanosheet Arrays on Carbon Cloth As an Efficient Bifunctional Electrocatalyst for Water Splitting in an Alkaline Electrolyte. *Dalton Trans.* **2020**, *49*, 5563-5572.
(82) Tang, C.; Zhang, R.; Lu, W.; He, L.; Jiang, X.; Asiri, A. M.; Sun, X. Fe-Doped CoP Nanoarray: A Monolithic Multifunctional Catalyst for Highly Efficient Hydrogen Generation. *Advanced Materials* **2017**, *29*, 1602441.
(83) Yan, Y.; Xia, B. Y.; Ge, X.; Liu, Z.; Fisher, A.; Wang, X. A Flexible Electrode Based on Iron Phosphide Nanotubes for Overall Water Splitting. *Chemistry-A European Journal* **2015**, *21*, 18062-18067.
(84) Aftab, F.; Duran, H.; Kirchhoff, K.; Zaheer, M.; Iqbal, B.; Saleem, M.; Arshad, S. N. A Facile Synthesis of FeCo Nanoparticles Encapsulated in Hierarchical N-Doped Carbon Nanotube/Nanofiber Hybrids for Overall Water Splitting. *ChemCatChem* **2020**, *12*, 932-943.
(85) Brillet, J.; Yum, J.-H.; Cornuz, M.; Hisatomi, T.; Solarska, R.; Augustynski, J.; Graetzel, M.; Sivula, K. Highly Efficient Water Splitting by a Dual-Absorber Tandem Cell. *Nature Photon* **2012**, *6*, 824-828.
(86) Shi, X.; Zhang, K.; Shin, K.; Ma, M.; Kwon, J.; Choi, I. T.; Kim, J. K.; Kim, H. K.; Wang, D. H.; Park, J. H. Unassisted Photoelectrochemical Water Splitting beyond 5.7% Solar-to-Hydrogen Conversion Efficiency by a Wireless Monolithic Photoanode/Dye-Sensitised Solar Cell Tandem Device. *Nano Energy* **2015**, *13*, 182-191.

(87) Luo, J.; Im, J.-H.; Mayer, M. T.; Schreier, M.; Nazeeruddin, M. K.; Park, N.-G.; Tilley, S. D.; Fan, H. J.; Grätzel, M. Water Photolysis at 12.3% Efficiency via Perovskite Photovoltaics and Earth-Abundant Catalysts. *Science* **2014**, *345*, 1593-1596.
(88) Chen, Y.-S.; Manser, J. S.; Kamat, P. V. All Solution-Processed Lead Halide Perovskite-$BiVO_4$ Tandem Assembly for Photolytic Solar Fuels Production. *J. Am. Chem. Soc.* **2015**, *137*, 974-981.
(89) Morales-Guio, C. G.; Mayer, M. T.; Yella, A.; Tilley, S. D.; Grätzel, M.; Hu, X. An Optically Transparent Iron Nickel Oxide Catalyst for Solar Water Splitting. *J Am Chem Soc* **2015**, *137*, 9927-9936.
(90) Gurudayal, null; Sabba, D.; Kumar, M. H.; Wong, L. H.; Barber, J.; Grätzel, M.; Mathews, N. Perovskite-Hematite Tandem Cells for Efficient Overall Solar Driven Water Splitting. *Nano Lett* **2015**, *15*, 3833-3839.
(91) Sharifi, T.; Larsen, C.; Wang, J.; Kwong, W. L.; Gracia-Espino, E.; Mercier, G.; Messinger, J.; Wågberg, T.; Edman, L. Toward a Low-Cost Artificial Leaf: Driving Carbon-Based and Bifunctional Catalyst Electrodes with Solution-Processed Perovskite Photovoltaics. *Advanced Energy Materials* **2016**, *6*, 1600738.
(92) Qiu, Y.; Liu, W.; Chen, W.; Chen, W.; Zhou, G.; Hsu, P.-C.; Zhang, R.; Liang, Z.; Fan, S.; Zhang, Y.; Cui, Y. Efficient Solar-Driven Water Splitting by Nanocone $BiVO_4$-Perovskite Tandem Cells. *Sci. Adv.* **2016**, *2*, e1501764.
(93) Liang, J.; Han, X.; Qiu, Y.; Fang, Q.; Zhang, B.; Wang, W.; Zhang, J.; Ajayan, P. M.; Lou, J. A Low-Cost and High-Efficiency Integrated Device toward Solar-Driven Water Splitting. *ACS Nano* **2020**, *14*, 5426–5434.
(94) Esiner, S.; van Eersel, H.; Wienk, M. M.; Janssen, R. A. J. Triple Junction Polymer Solar Cells for Photoelectrochemical Water Splitting. *Advanced Materials* **2013**, *25*, 2932–2936.
(95) Kumar, A.; Chaudhary, D. K.; Parvin, S.; Bhattacharyya, S. High Performance Duckweed-Derived Carbon Support to Anchor NiFe Electrocatalysts for Efficient Solar Energy Driven Water Splitting. *J. Mater. Chem. A* **2018**, *6*, 18948-18959.
(96) Ma, L.; Zhang, W.; Zhao, P.; Liang, J.; Hu, Y.; Zhu, G.; Chen, R.; Tie, Z.; Liu, J.; Jin, Z. Highly Efficient Overall Water Splitting Driven by All-Inorganic Perovskite Solar Cells and Promoted by Bifunctional Bimetallic Phosphide Nanowire Arrays. *J. Mater. Chem. A* **2018**, *6*, 20076-20082.
(97) Liu, X.; Huang, P.; Dong, Q.; Wang, Z.; Zhang, K.; Yu, H.; Lei, M.; Zhou, Y.; Song, B.; Li, Y. Enhancement of the Efficiency and Stability of Planar p-i-n Perovskite Solar Cells via Incorporation of an Amine-Modified Fullerene Derivative as a Cathode Buffer Layer. *Sci. China Chem.* **2017**, *60*, 136-143.
(98) Reece, S. Y.; Hamel, J. A.; Sung, K.; Jarvi, T. D.; Esswein, A. J.; Pijpers, J. J. H.; Nocera, D. G. Wireless Solar Water Splitting Using Silicon-Based Semiconductors and Earth-Abundant Catalysts. *Science* **2011**, *334*, 645-648.
(99) Xin, Y.; Kan, X.; Gan, L.-Y.; Zhang, Z. Heterogeneous Bimetallic Phosphide/Sulfide Nanocomposite for Efficient Solar-Energy-Driven Overall Water Splitting. *ACS Nano* **2017**, *11*, 10303-10312.